REFERENCES

[1] S. Glashow, Nucl. Phys. 22, 529 (1961);
S. Weinberg, Phys. Rev. Lett. 19, 1264 (1967);
A. Salam, in Elementary Particle Theory, edited by N. Svartholm (Almqvist & Wiksell, Stockholm, 1968)

[2] F. Scheck, Phys. Lett. C44, 187 (1978)

[3] A. Jodidio et al., Phys. Rev. D34, 1967 (1986);
D.P. Stoker et al., Phys. Rev. Lett. 54, 1887 (1985)
J. Carr et al., Phys. Rev. Lett. 51, 627 (1983)

[4] D. Fryberger, Phys. Rev. 166, 1379 (1968)

[5] We ignore finite W_L mass effects. This implies (negligible) corrections of $O(m_\mu^2/m_W^2)$.

[6] Particle Data Group, C.G. Wohl et al., Phys. Lett. 170B (1986).
Primary input to ρ is from J. Peoples, Nevis Cyclotron Report No. 147, 1966 (unpublished);
primary input to η is from F. Corriveau et al., Phys. Lett. 129B, 260 (1983) and S.E. Derenzo, Phys. Rev. 181, 1854 (1969);
primary input to ξP_μ is from V.V. Akhmanov et al., Yad. Fiz. 6, 316 (1967);
primary input to δ is from Ref. 4;

primary input to $\xi P_\mu \delta/\rho$ is Ref. 3.

[7] A.M. Sachs and A. Sirlin, in Muon Physics, Vol. III, V. Hughes and C.S. Wu, eds. (Academic Press, N.Y., 1975), p.50

[8] Y.S. Tsai, Stanford Linear Accelerator Pub. No. SLAC-PUB-848 (1971), App. B.

[9] H.W. Koch and J.W. Motz, Rev. Mod. Phys. 31, 920 (1959)

[10] C.J. Oram, J.B. Warren, G.M. Marshall and J. Doornbos, Nucl. Instrum. Methods 179, 95 (1981)

[11] D.A. Ross, Nuovo Cimento 10A, 475 (1972);
A.V. Kuznetsov and N.V. Mikheev, Yad. Fiz. 31, 258 (1979)

[12] For magnet monitoring, we used NMR probes developed by R. Openshaw at TRIUMF (three different models were needed to cover the range from 600 to 4200 G), and commercial Hall probes by F.W. Bell (Models BH-701 (high sensitivity, linear to 0.1%), BH-702 (concentrator), and BH-705).

[13] D.P. Stoker, Ph.D. Thesis, Lawrence Berkeley Laboratory Report No. LBL-20324, 1985 (unpublished)

[14] W.P. Trower, Lawrence Radiation Laboratory Report No. UCRL-2426, 1966

[15] R.M. Sternheimer, Phys. Rev. 117, 485 (1960)

[16] K. Halbach (private communication). In the first-order optics appoximation, the radial component of the field off-axis is estimated from the gradient of the longitudinal field on-axis. See App. A of Ref. 13 for details.

[17] F. James and M. Roos, CERN Computer Center Reports Nos. D506 and D516 (unpublished).

[18] R. Kubo and K. Tomita, J. Phys. Soc. Jpn 9, 888 (1954)

[19] M.J. Berger and S.M. Seltzer, "Stopping Powers and Ranges of Electrons and Positrons" (2nd Ed.), U.S. National Bureau of Standards Report NBSIR 82-2550-A (1982)

[20] K.W. Kehr et al., Z. Phys. B32, 49 (1978)

[21] D. Richter, in Neutron Scattering and Muon Spin Rotation, Springer Tracts in Modern Physics 101 (Springer-Verlag 1983) p.85

[22] K. Mursula and F. Scheck, Nucl. Phys. B253, 189 (1985)

[23] H. Burkard et al., Phys. Lett. B160, 343 (1985)

[24] W. Fetscher, H.-J. Gerber, and K.F. Johnson, Phys. Lett. 173B, 102 (1986);
D.P. Stoker in AIP Conference Proceedings No. 150, "Intersections Between Particle and Nuclear Physics", Lake Louise (1986), p.976

[25] B. Balke et al., Lawrence Berkeley Laboratory Report No. LBL-18320, 1984 (unpublished)

[26] H.P. Nilles, Phys. Rep. 110, 1 (1984)

[27] J.C. Pati and A. Salam, Phys. Rev. D 10, 275 (1974);
R.N. Mohapatra and J.C. Pati, ibid. 11, 566 (1974); 11, 2558 (1974);
G. Senjanovic and R.N. Mohapatra, ibid. 12, 1502 (1975);
G. Senjanovic, Nucl. Phys. B135, 334 (1979)

[28] As concerns supersymmetry, see H. Haber and G. Kane, Phys. Rep. 117, 75 (1985);
S. Dawson, Nucl. Phys. B261, 297 (1985)

[29] K. Mursula, M. Roos, and F. Scheck, Nucl. Phys B219, 321 (1983);
K. Mursula, ibid. B241, 173 (1984)

[30] W. Buchmuller and F. Scheck, Phys. Lett. 145B, 421 (1984)

[31] C. Hearty, et al., Stanford Linear Accelerator Pub. No. SLAC-PUB-4114 (1987);
C. Hearty, private communication.

[32] D. Reiss, Phys. Lett. 115B, 217 (1982);
F. Wilczek, Phys. Rev. Lett. 49, 1549 (1982)

[33] D.A. Bryman and E.T.H. Clifford, Phys. Rev. Lett. 57, 2787 (1986)

[34] E. Eichten, Fermilab National Accelerator Laboratory pub. FERMILAB-Conf-85/178-T, 1986

[35] A.I. Boothroyd, J. Markey, and P. Vogel, Phys. Rev. C 29, 603 (1984)

[36] L. Landau, J. Phys. (U.S.S.R.) 8, 201 (1944)

[37] F. Rohrlich and B.C. Carlson, Phys. Rev. 93, 38 (1954)

[38] R.E. Shrock, Phys. Rev. D 24, 1275 (1981)

[39] Particle Data Group, C.G. Wohl et al., Phys. Lett. 170B, 53 (1986)

TABLE 1. **Muon Decay Parameters.** Standard model ('V-A') theoretical values and experimental values of the parameters in Eq. II.1.

	V-A	Expt
ρ	0.75	0.7517 ± 0.0026
η	0	0.06 ± 0.15
δ	0.75	0.7551 ± 0.0085
ξP_μ	1	0.972 ± 0.14
$\xi P_\mu \delta/\rho$	1	$0.9975 < \xi P_\mu \delta/\rho < 1$ (90% CL)

TABLE 2. Spectrometer Momentum Resolution. Results of the relative calibration of Sec. V.A using the endpoint of the muon decay spectrum (Fig. 15). Φ_s is the spectrometer field scale factor relative to B_s=3186.7 G. $y_{r,\mu e} = 0.9917/\Phi_s$ is the expected relative momentum of decay endpoint, y_r is the fit endpoint momentum and σ_y the fit resolution. The difference between the second and third columns is due to a combination of statistical fluctuations, spectrometer non-linearity and fringe field effects.

Φ_s	$y_{r,\mu e}$	y_r	σ_y
1.17	0.8476	0.8484(4)	0.0023(4)
1.13	0.8776	0.8779(2)	0.0021(2)
1.09	0.9098	0.9092(3)	0.0017(3)
1.05	0.9445	0.9440(2)	0.0011(3)
1.00	0.9917	0.9919(2)	0.0008(3)
0.95	1.0438	1.0445(3)	0.0011(4)
0.92	1.0779	1.0796(3)	0.0016(4)
0.88	1.1269	1.1282(4)	0.0020(3)
0.85	1.1666	1.1694(4)	0.0016(4)

TABLE 3. Systematic Effects in the Beamline. Variation in the beamline momentum setting Y_b with the beamline parameters. 'Least Count' refers to the resolution of the digital beamline control system when setting a given parameter. For the magnets, the percentages are of the Y_b=1.00 current. For comparison, the systematic error on the calibration data points was σ_Y=0.0005.

Parameter	Least Count	$\Delta Y_b/Y_b$	ΔY_b
1AT1 proton spot moved	≈1mm	<0.00024	
Horiz. Jaw Center	1mm	-0.00002	
SL1 Center	0.1mm	-0.00005	
SL1, SL2 Width	0.1,0.1mm	0.00000	
SL2 Center	0.1mm	0.00005	
Q1 Current	0.5%		0.00002
Q2 Current	0.8%		0.00012
Q4 Current	0.5%		0.00002
Q6 Current	1%		0.00013
Q7 Current	0.8%		0.00017
B2	0.05%		0.0006

TABLE 4. Calibration Combinations. The calibration fits used in the analysis. 'E' and 'L' refer respectively to the early and later calibration data sets and π-μ measurements. The results of the asymmetry fits over the six calibration (excluding N_f=2) were averaged to obtain the final results, and the calibration errors were determined by taking differences between the calibrations as indicated.

N_f	Data	π-μ	Magnet	Peak	Comment
1	E	L	B1	y_r(ave)	'Standard' Earlier Calibration
2	E	E	B1	y_r(fit)	Checks beamline gaussian momentum distribution assumption
3	E	L	B1	y_r(ave)	$\pi\mu$ reproducibility (with 1)
4	E	E	B2	y_r(ave)	Beam μ^+-e^+ differences (with 1)
5	L	L	B1	y_r(ave)	'Standard' Later Calibration
					y_r correction reproducibility (with 3)
6	L	E	B1	y_r(ave)	$\pi\mu$ reproducibility (with 5)
					y_r correction reproducibility (with 1)
7	L	L	B2	y_r(ave)	Beam μ^+-e^+ differences (with 5)

TABLE 5. μSR Time Parameters. The fitted values of the parameters which describe the time dependence of the μSR decay spectrum. 'First' and 'Second' refer to muon decay clock in use when the data fitted was taken. 'Combined' refers to the total sample with the clock readouts brought into agreement using the fit values of τ_μ and t_0. 'F' and 'S' refer to fast and slow precession frequencies. For comparison, in the third column we scale ω and G for the second clock to equivalent first clock results using the ratio of the measured lifetimes.

	First	Second	→ First	Combined
τ_μ [μsec]	2.200(8)	2.180(10)		
t_0,F	0.4484(10)	0.4357(7)		
,S [μsec]	0.4464(8)	0.4352(6)		
ω,F	9.575(3)	9.652(14)	9.566	9.571(3)
,S [μsec]$^{-1}$	5.929(2)	5.983(12)	5.930	5.929(2)
G,F	0.0030(4)	0.0028(4)	0.0028	0.0029(3)
,S [μsec]$^{-2}$	0.0036(4)	0.0039(5)	0.0038	0.0036(3)

TABLE 6a. Asymmetry Fits. The energy range and fit statistics for each of the four data sets. Φ_S indicates the spectrometer field strength; 'AL' and 'TA' indicate thick and thin target samples, respectively; 'F' and 'S' indicate fast and slow muon spin precession frequency samples. The events (Evts), χ^2 and degrees of freedom (DOF) entries are in units of 10^3. The expected Poisson maximum-likelihood χ^2 is 2/DOF.

		AL,F		AL,S		TA,F		TA,S		
Φ_S	x	Evts	χ^2	Evts	χ^2	Evts	χ^2	Evts	χ^2	DOF
0.42	0.36-0.42	42	2.3	43	2.5	35	2.3	35	2.4	1.0
0.50	0.44-0.60	57	3.2	52	3.1	44	3.1	46	3.0	1.4
0.60	0.52-0.72	74	3.8	66	3.9	54	4.0	54	3.8	1.8
0.72	0.60-0.84	68	4.6	64	4.5	55	4.6	54	4.6	2.2
0.86	0.72-1.00	78	5.2	74	5.5	70	5.6	66	5.3	2.6
1.00	0.84-1.00	35	3.2	34	3.1	29	3.2	27	3.1	1.4

TABLE 6b. Asymmetry Fit Results. The fit asymmetry M(x) by target type and precession frequency for the calibration fit (N_f=6) that was nearest the average of those in Tbl. 4. ΔM is the adjustment applied to the measured asymmetries to cancel the effects of external radiative corrections.

			M(x)		
Tgt	Φ_S	x	F	S	ΔM
AL	0.42	0.37	-0.065(22)	-0.101(22)	-0.0099
		0.39	-0.067(19)	-0.076(19)	-0.0082
		0.41	-0.047(17)	-0.059(17)	-0.0085
		0.43	-0.018(17)	-0.032(16)	-0.0080
		0.45	-0.014(16)	-0.049(16)	-0.0079
		0.47	-0.004(16)	0.004(16)	-0.0078
	0.50	0.45	0.001(22)	-0.005(23)	-0.0068
		0.47	0.004(19)	0.012(20)	-0.0070
		0.49	0.019(17)	0.015(18)	-0.0067
		0.51	0.022(16)	0.013(17)	-0.0070
		0.53	0.034(16)	0.076(17)	-0.0067
		0.55	0.045(16)	0.072(17)	-0.0068
		0.57	0.105(17)	0.060(17)	-0.0066
		0.59	0.138(18)	0.147(19)	-0.0068
	0.60	0.53	0.028(22)	0.058(22)	-0.0077
		0.55	0.084(19)	0.067(20)	-0.0070
		0.57	0.087(17)	0.085(18)	-0.0064
		0.59	0.087(17)	0.125(17)	-0.0065
		0.61	0.116(16)	0.125(17)	-0.0076
		0.63	0.166(16)	0.175(16)	-0.0070
		0.65	0.181(16)	0.193(16)	-0.0071
		0.67	0.235(16)	0.236(16)	-0.0073
		0.69	0.257(17)	0.238(19)	-0.0075
		0.71	0.254(18)	0.287(19)	-0.0061

	0.72	0.61	0.140(27)	0.125(28)	-0.0079
		0.63	0.145(24)	0.149(24)	-0.0080
		0.65	0.210(22)	0.198(22)	-0.0081
		0.67	0.217(20)	0.223(20)	-0.0074
		0.69	0.246(19)	0.270(19)	-0.0070
		0.71	0.257(18)	0.285(18)	-0.0069
		0.73	0.305(17)	0.309(17)	-0.0067
		0.75	0.335(17)	0.349(17)	-0.0071
		0.77	0.368(17)	0.352(17)	-0.0065
		0.79	0.395(18)	0.453(17)	-0.0070
		0.81	0.441(18)	0.452(17)	-0.0064
		0.83	0.486(18)	0.495(18)	-0.0064
	0.86	0.73	0.296(26)	0.308(25)	-0.0091
		0.75	0.347(24)	0.366(23)	-0.0084
		0.77	0.430(21)	0.363(20)	-0.0073
		0.79	0.414(18)	0.404(19)	-0.0078
		0.81	0.434(17)	0.465(18)	-0.0077
		0.83	0.507(16)	0.515(16)	-0.0071
		0.85	0.526(16)	0.557(15)	-0.0067
		0.87	0.608(15)	0.608(14)	-0.0065
		0.89	0.641(15)	0.654(14)	-0.0062
		0.91	0.644(15)	0.690(14)	-0.0061
		0.93	0.729(15)	0.750(14)	-0.0057
		0.95	0.809(15)	0.822(13)	-0.0052
		0.97	0.855(13)	0.868(13)	-0.0045
		0.99	0.936(13)	0.942(12)	-0.0013
	1.00	0.85	0.548(25)	0.524(24)	-0.0076
		0.87	0.610(22)	0.572(21)	-0.0073
		0.89	0.633(21)	0.623(20)	-0.0064
		0.91	0.695(19)	0.671(18)	-0.0067
		0.93	0.723(17)	0.731(16)	-0.0058
		0.95	0.838(15)	0.806(12)	-0.0054
		0.97	0.879(13)	0.879(12)	-0.0047
		0.99	0.944(12)	0.966(10)	-0.0014
TA	0.42	0.37	-0.064(25)	-0.083(25)	-0.0115
		0.39	-0.094(21)	-0.107(21)	-0.0097
		0.41	-0.055(19)	-0.062(19)	-0.0100
		0.43	-0.043(18)	-0.041(18)	-0.0094
		0.45	-0.006(18)	-0.014(17)	-0.0092
		0.47	0.009(18)	0.001(17)	-0.0091
	0.50	0.45	-0.018(25)	0.001(24)	-0.0081
		0.47	0.010(22)	0.007(21)	-0.0083
		0.49	-0.031(20)	0.015(19)	-0.0079
		0.51	0.041(19)	0.030(18)	-0.0082
		0.53	0.049(19)	0.054(18)	-0.0078
		0.55	0.060(18)	0.054(18)	-0.0079
		0.57	0.075(19)	0.100(18)	-0.0077
		0.59	0.117(21)	0.116(20)	-0.0078

0.60	0.53	0.081(25)	0.084(25)	-0.0088
	0.55	0.088(22)	0.036(22)	-0.0081
	0.57	0.097(21)	0.135(20)	-0.0075
	0.59	0.127(20)	0.134(19)	-0.0075
	0.61	0.128(19)	0.144(18)	-0.0076
	0.63	0.176(18)	0.162(18)	-0.0070
	0.65	0.192(18)	0.185(18)	-0.0079
	0.67	0.199(19)	0.211(18)	-0.0081
	0.69	0.203(20)	0.265(19)	-0.0073
	0.71	0.272(21)	0.285(21)	-0.0069
0.72	0.61	0.143(30)	0.093(29)	-0.0089
	0.63	0.155(28)	0.156(27)	-0.0090
	0.65	0.200(25)	0.225(24)	-0.0090
	0.67	0.210(23)	0.238(22)	-0.0083
	0.69	0.223(21)	0.266(20)	-0.0078
	0.71	0.277(20)	0.284(19)	-0.0077
	0.73	0.305(19)	0.294(19)	-0.0075
	0.75	0.312(19)	0.361(18)	-0.0078
	0.77	0.332(19)	0.412(18)	-0.0072
	0.79	0.408(19)	0.420(19)	-0.0077
	0.81	0.456(20)	0.493(18)	-0.0070
	0.83	0.506(20)	0.504(19)	-0.0070
0.86	0.73	0.285(27)	0.339(26)	-0.0091
	0.75	0.342(25)	0.333(24)	-0.0092
	0.77	0.384(23)	0.437(22)	-0.0080
	0.79	0.418(21)	0.437(20)	-0.0085
	0.81	0.476(19)	0.489(18)	-0.0083
	0.83	0.489(18)	0.491(17)	-0.0077
	0.85	0.553(17)	0.623(16)	-0.0072
	0.87	0.590(17)	0.594(15)	-0.0069
	0.89	0.630(17)	0.645(15)	-0.0066
	0.91	0.699(16)	0.691(15)	-0.0064
	0.93	0.750(16)	0.756(14)	-0.0059
	0.95	0.833(14)	0.785(14)	-0.0053
	0.97	0.883(14)	0.836(14)	-0.0045
	0.99	0.941(13)	0.924(13)	-0.0012
1.00	0.85	0.548(27)	0.520(26)	-0.0081
	0.87	0.608(24)	0.602(25)	-0.0077
	0.89	0.646(22)	0.622(22)	-0.0068
	0.91	0.704(20)	0.722(19)	-0.0070
	0.93	0.772(18)	0.763(17)	-0.0060
	0.95	0.808(17)	0.804(16)	-0.0055
	0.97	0.868(15)	0.846(14)	-0.0047
	0.99	0.952(13)	0.955(11)	-0.0013

TABLE 7. Decay Parameter Fits. The upper part of the table exhibits the decay parameter fit results to the data of Tbl. 6b by target type and precession frequency. The TA/S data contained a single point with χ^2 of 25 whose removal did not affect the fit results. The lower half exhibits the fit results for the combined data for each of the seven calibrations of Tbl. 4. N_f = 6 corresponds to the combined upper half data. The calibration N_f=2 was not included in the combined average.

Target	ω	δ	ξP_μ	χ^2/DOF
AL	F	0.7491(51)	0.9734(67)	56/55
AL	S	0.7481(50)	0.9866(67)	47/55
TA	F	0.7562(56)	0.9763(75)	38/55
TA	S	0.7370(54)	0.9954(72)	90/55

N_f	δ	ξP_μ	χ^2/DOF
1	0.7467(26)	0.9850(35)	240/229
2	0.7466	0.9851	
3	0.7475	0.9837	
4	0.7473	0.9846	
5	0.7486	0.9815	
6	0.7477	0.9829	
7	0.7494	0.9804	
(except 2)	0.7479(26)	0.9830(35)	

TABLE 8. Decay Parameters: Systematic Errors and Corrections

Source	$\Delta\delta \pm \sigma_\delta$ ($\times 10^4$)	$\Delta\xi P_\mu \pm \sigma_\xi$ ($\times 10^4$)
Momentum Calibration		
$\pi\mu$ Reproducibility	± 9	±14
μ-e Differences	± 8	± 8
y_r Corrections	±11	±22
Total	±20	±31
Momentum Resolution	± 2	±13
Radiative Corr.	±16	±22
Energy Loss Calculation	± 3	± 3
Muon Scattering and Contamination		15± 5
TOTAL	0±26	19±41
World value ρ	7±11	12±17
TOTAL	7±28	31±44

TABLE 9. Limits on Alternative Couplings 90% C.L. limits on the contributions of non-standard model couplings $g^i_{\alpha\beta}$ to the muon decay Hamiltonian and the muon decay rate (final column). i is the Lorentz structure of the coupling, α and β respectively indicate the handedness of the muon and electron currents (Sec. VIII.1).

i	α	β	$\lvert g^i_{\alpha\beta}\rvert$ ($\times 10^{-3}$)	B.R.
S	R	R	< 66	< 0.1 %
S	L	R	<125	< 0.25%
S	R	L	<424	< 2.5 %
S	L	L	<918	<20 %
T	R	L	<122	< 4 %
T	L	R	< 36	< 0.4 %
V	R	R	< 33	< 0.1 %
V	L	R	< 60	< 0.25%
V	R	L	<110	< 1 %
V	L	L	>888	>79 %

TABLE 10. Momentum Calibration Results. The fit results to the early and late calibration data of Sec. V and Fig. 17, with the spectrometer zero-point B_{s_0} indicated by the bending magnet B1 or B2 used to calibration the beamline. The fit errors on the parameters were small compared to the early-late differences. The fit values of a and b were essentially unchanged after the switch from B1 to B2.

	Data and $\pi\mu$ Calibration Set	
	Earlier	Later
a	$(-1.2-0.6Y_S)\times10^{-3}$	$(-2.5-16.3Y_S)\times10^{-3}$
b	$-0.048-0.001Y_S$	$-0.013-0.042Y_S$
B1 Beamline Calibration		
B_{s_0}	16.6 G	8.4 G
$B1_0$	2.7 G	-1.7 G
$B1_{\pi\mu}$	875.6 G	874.8 G
χ^2/DOF	38/33	31/33
B2 Beamline Calibration		
B_{s_0}	13.3 G	3.4 G
$B2_0$	0.4 G	-3.4 G
$B2_{\pi\mu}$	954.3 G	952.6 G
χ^2/DOF	30/33	39/33

Fig. 1. Muon Decay Diagrams: Unless explicitly marked, all bosonic (wavy) lines are photons. a) Tree-level Feynman diagrams for muon decay. The standard model decay is on the left. In the limit $(m_\mu/M_W)\to 0$, we obtain the four-fermi contact interaction diagram on the right. Equation II.1 follows from the generalization of this diagram to all possible fermion couplings. b) First-order QED internal radiative corrections to muon decay. c) External radiative corrections: interactions of the final-state positron with the material of the apparatus. Bremsstrahlung is on the left, Bhabba scattering on the right.

Fig. 2. Muon Decay Spectrum: The standard model differential muon decay rate in x and $\cos\theta$ versus the reduced positron energy x for $\cos\theta = +1$, -1 and 0 (unpolarized curve), where $\pi-\theta$ is the angle beteen the positron direction and the muon spin. Internal radiative corrections to first order are included throughout, second-order effects only near the decay endpoint at x=1.00. The degree of parity violation is found from the difference of the forwards and backwards curves divided by twice the unpolarized curve.

Fig. 3. M13 Beamline: B1 and B2 are bending magnets, Q1-Q7 are quadrupoles. All magnets were thick lenses, the combinations Q1-Q2 and Q6-Q7 forming focusing doublets and Q3-Q4-Q5 forming a focusing triplet. F1, F2 and F3 indicate focal points of the source at 1AT1; S1, S2 and the jaws after Q2 were apertures. The beam envelope was

asymmetric about Q4. The final focus F3 coincides with the "Tgt" in Fig. 4.

Fig. 4. Experimental Apparatus P1-P3 and A are proportional chambers; S1-S3 are scintillators; D1-D4 are drift chambers. Veto scintillators V1 and V2 surrounding S1 and S2 respectively are not shown. Muons are stopped in the target, and decay positrons are focused by the solenoid magnet into the spectrometer.

Fig. 5. Zero Point of the Decay Asymmetry: The muon decay asymmetry M(x) vs. the reduced positron energy x near its zero point at x_z ($M(x_z)=0$). The "Michel" spectrum is the standard model prediction without radiative corrections. The other curves indicate the effect on M(x) of the radiative corrections of Figs. 1b and 1c. In calculating the external radiative effects, the simplifying assumptions were made that positrons moved parallel to the solenoid field and that the event reconstruction and analysis had no biases against energy straggling. A realistic Monte Carlo simulation of the experiment reproduced only ≈70% of the shift in x_z seen here due to external radiative corrections.

Fig. 6. M13 Positive-Particle Flux: Flux in the M13 beamline at TRIUMF of the different particle species versus beamline momentum setting (adapted from Ref. 26). The data were collected with all slits and jaws in the beamline fully open. The dramatic decreases in muon flux

at 29.79 MeV/c (highest momentum for muons from π^+ decay at rest in 1AT1) and positron flux at 52.83 MeV/c (highest momentum for e^+ from μ^+ decay at rest in 1AT1) were potential beamline calibration points.

Fig. 7. Reconstructed Beam Momentum Distribution: Measured beam positron spectrum in intervals $\Delta y=0.001$ versus the reduced positron momentum y. The long tail results from energy straggling in 260 mg/cm^2 of material between the M13 vacuum window and the spectrometer. The curve is a fit of the data to a straggled gaussian with initial FWHM $\Delta y/y=0.6\%$. Broadening at the spectrometer by energy straggling and spectrometer resolution is evident. For the data, the peak measures of Sec. V.B.3 are y(ave)=0.9928 and y(fit)=0.9930; for the curve y(ave)=0.9927 and y(fit)=0.9933.

Fig. 8. Beam Positron Envelopes at F3: The phase space distributions of beam positrons in the focal plane at F3 for the coordinate pairs: a) (u,v), b) (u',v'), c) (u,u') and d) (v,v'). The coordinates are for a cartesian system with w along the beam axis, u horizontal and v vertical, u'=du/dw and v'=dv/dw. Peaking in u and v, due to the discrete resolution of P3, has been suppressed to emphasize the fringes of the distributions. The (u,u') and (v,v') correlations are an artifact of the curved track fit.

Fig. 9. Beam Positron Momentum Correlations at F3: See also the caption for Fig. 8. a) Reduced momentum y of beam positrons versus the vertical slope v' at F3. Cuts were made at v' = ±0.05 rad. b) Reduced positron momentum versus the horizontal coordinate u at F3. b) and Fig. 10 indicate the presence of unexpected material in the target area near S1. Cuts were made at u = ±0.7 cm.

Fig. 10. Decay Positron Spot: See also the caption for Fig. 8. The distribution of decay positrons in intervals Δu=0.004 cm versus the horizontal coordinate u at F3. The lack of counts at low u indicates that muons at low u were stopped before reaching the target by extra material near S1.

Fig. 11. Spectrometer Field Map: Strength in kG of the components of the spectrometer field versus radius r from the magnet center. z is the vertical coordinate in the cylindrical system with origin at the magnet center. B_z is the vertical field in the magnet midplane, ΔB_z is the change in vertical field strength at z=8 cm, B_r is the radial field strength at that same displacement from the midplane. The last two components varied with z as $\Delta B_z \propto z^2$, $B_r \propto z$.

Fig. 12. Trigger Logic Diagram: Fast logic used to distinguish μ stop, μ decay and beam positron straight through ("st thru") events. The logic inputs are labelled by detector: the combined output of the A proportional chamber, the U and V planes of proportional chambers P1-P3, plane or the left-right (L or R) photomultiplier tube output for scintillators S1-S2, V1 and V2. The six G inputs represent the L-R output of the three vertical segments of scintillator S3. The Busy signal disabled the trigger while the online analysis read the data registers and wrote an event to tape.

Fig. 13. Extra Cuts: Spectrum of decay positrons in intervals $\Delta y=0.001$ versus the reduced positron momentum y, showing contamination by beam positrons near $y=0.55$ (upper curve). Applying "extra after" cuts (middle curve, Sec. IV.A) eliminated the beam positron peak, isolating a pure μ-decay sample. The "extra before" cuts (lower curve) rejected decays observed while multiple muons were in the target. The final sample was free of events composed of signals from unrelated muons and positrons.

Fig. 14. Momentrum Reconstruction Schematic: Simulated positron track from D3 to D4 through the spectrometer, illustrating one iteration of the reconstruction algorithm of Sec. V.C. The spectrometer field (Fig. 11) was divided into three regions (central, bump and fringe) with boundaries at radii r of 36, 51 and 86 cm (circular arcs).
a) Vertical projection of the positron motion, showing the change in

the vertical slope made at r=51 cm to simulate the effect of the radial component of the field. b) The positron motion projected into the midplane of the spectrometer. The radius of curvature of the track was allowed to change only at the circular boundaries. The difference Δu between the forward (solid) and backward (dashed) extrapolations of the track at the exit focal plane was used to re-estimate the momentum using the known spectrometer dispersion.

Fig. 15. Momentum Resolution Fits: Decay positron spectrum in intervals $\Delta y=0.001$ versus the reduced momentum y near the muon decay endpoint. The graphs (a-c) represent data taken with the spectrometer central field scaled from 3186.7 G by Φ_S = 1.17, 1.00 and 0.85, respectively, correspond to fits one, five and nine of Tbl. 2. The fit to the data, which extended to lower y than is shown, is described in Sec. V.A.

Fig. 16. π-μ Calibration: See also the caption to Fig. 6. The fraction of the flux in M13 represented by muons ((μ STOP)/(BEAM)) as the central field strength in B1 was varied near the π-μ calibration point. a and b show the earlier and later π-μ calibrations, respectively.

Fig. 17. Momentum Calibration Results: See the text of Sec. V.B.4 for a detailed discussion of the fit results, and App. B for a discussion of the fit to the data points. On the left (right) are the results of the fit to the earlier (later) calibration data. The upper graphs a) and b) show the fitted corrections to the center Y_b of the momentum distribution transmitted by the beamline versus field strength in the bending magnet B1. The triangles are the π-μ calibration points, and the circles correspond to the data points nearest the vertical line in the lower graphs. The lower graphs c) and d) show the final corrections to the initial momentum reconstruction $y_r\Phi_s$ (vertical axis) vs. the particle momentum y normalized to the spectrometer momentum setting Y_s for each of the six values of the spectrometer field $B_s = 3186.7\ \Phi_s$ G ($\Phi_s = Y_s$ if the spectrometer zero-point offset is zero). Δx is the energy (or momentum) lost by the positrons before reaching the spectrometer. The six sets of polygonal data points represent the beam positron calibration data taken with Φ_s=1.00 (open circles), 0.86 (filled circles), 0.72 (open squares), 0.60 (filled squares), 0.50 (open triangles) and 0.42 (filled triangles). For clarity these data have been displace downwards by 0, 0.0025, 0.005, 0.0075, 0.01 and 0.0125, respectively. The crosses at Φ_s=1.00 are the data in Tbl. 2 from the decay endpoint calibration of Sec. V.A.

Fig. 18. Spin-Held Decay Rate: Time spectrum (counts in intervals Δt=0.08 μsec versus the muon decay time t in μsec) of the spin-held data collected with the first muon decay clock. The suppression at early times was due to self-vetoing of events soon after the muon

arrival by ringing in the μ-arm proportional chamber output. The unbiased time range ran from 1.4 to 8.8 μsec. The fit muon decay lifetime for data in this interval was τ_μ = 2.200(8) μsec; the accepted value is τ_μ = 2.197 μsec.

Fig. 19. μSR Decay Rate: Counts in intervals Δt=0.08 μsec versus the muon decay time t in μsec for the μSR (spin-precessed) data. These combined fast (upper) and slow (lower) precession frequency data were used to determine the time constants which described the μSR signal. Only the time range fit is shown.

Fig. 20. Asymmetry Fits: The μSR component of the muon decay rate in intervals Δt=0.08 μsec versus the muon decay time t for fast and slow precession frequency data, illustrating the fit for the decay asymmetry M(x). R(ani) is the parity violating term (with ξ) in Eq. II.3, R(iso) is the parity conserving term. a-c are "fast" precession frequency data, d-f are "slow". The curves a and d show maximum parity violation in the energy range 0.96-1.00. The curves b and e, including energies from x=0.44-0.48, are near the zero point of the asymmetry. The asymmetry changes sign in the lowest energy bin (c and f, x=0.36-0.40). Only the time range fit is shown.

Fig. 21. Fit for Muon Decay Parameters The lower plot shows the fit muon decay asymmetry M(x) versus the reduced positron energy x. The 32 data points represent the combined measurements of Tbl. 6b, and the curve is the fit to (II.8) with δ=0.7479 and ξP_μ=0.9830. The upper plot shows the statistical errors and fit residuals for the 32 data points.

Fig. 22. W_R Mass Limits 90% C.L. limits on the mass of a hypothetical guage boson W_R versus the right-handed muon neutrino mass $m(\nu_{\mu R})$ in left-right symmetric extensions of the standard model of the weak interactions. The area below the curves is disallowed. The strong limits shown as peaks near near $m(\nu_{\mu R})$=0 are from the analysis of Ref. 3.

Fig. 23. Wino Mass Limits 90% C.L. limits on the mass of the $\tilde{W}$ versus the mass of the muon sneutrino in supersymmetric extensions of the standard model of the weak interactions. The area below the curves is disallowed. The horizontal line at $M(\tilde{W})$ = 61 GeV represents the limits of Ref. 31.

Fig. 24. Limits on the Scalar Decay $\mu \to e\sigma$ a) The number of muon decay events in intervals Δx=0.001 versus the reduced positron energy x. Only every fifth bin is plotted. This spectrum was searched for peaks indicating the decay $\mu \to e\sigma$. The discontinuities reflect the edges of

the calibrated energy range at different values of the spectrometer central field. b) 90% C.L. limits on the branching ratio for the decay $\mu \to e\sigma$ versus the mass of the σ particle. The forbidden region lies above the curves. Also sketched (smooth curves) are the limits obtained in Ref. 33 using a similar analysis of earlier data.

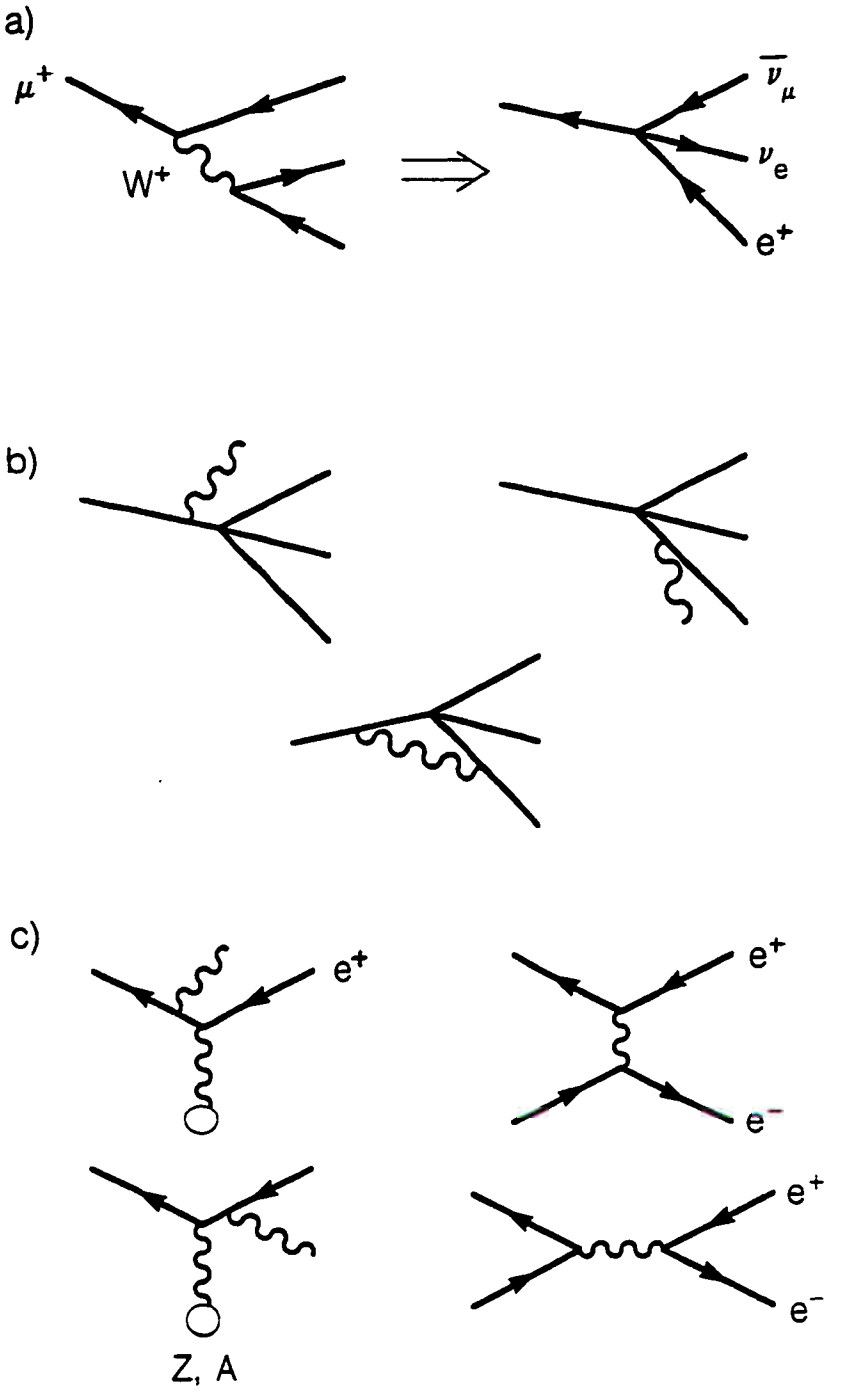

XBL 873-9618

Fig. 1

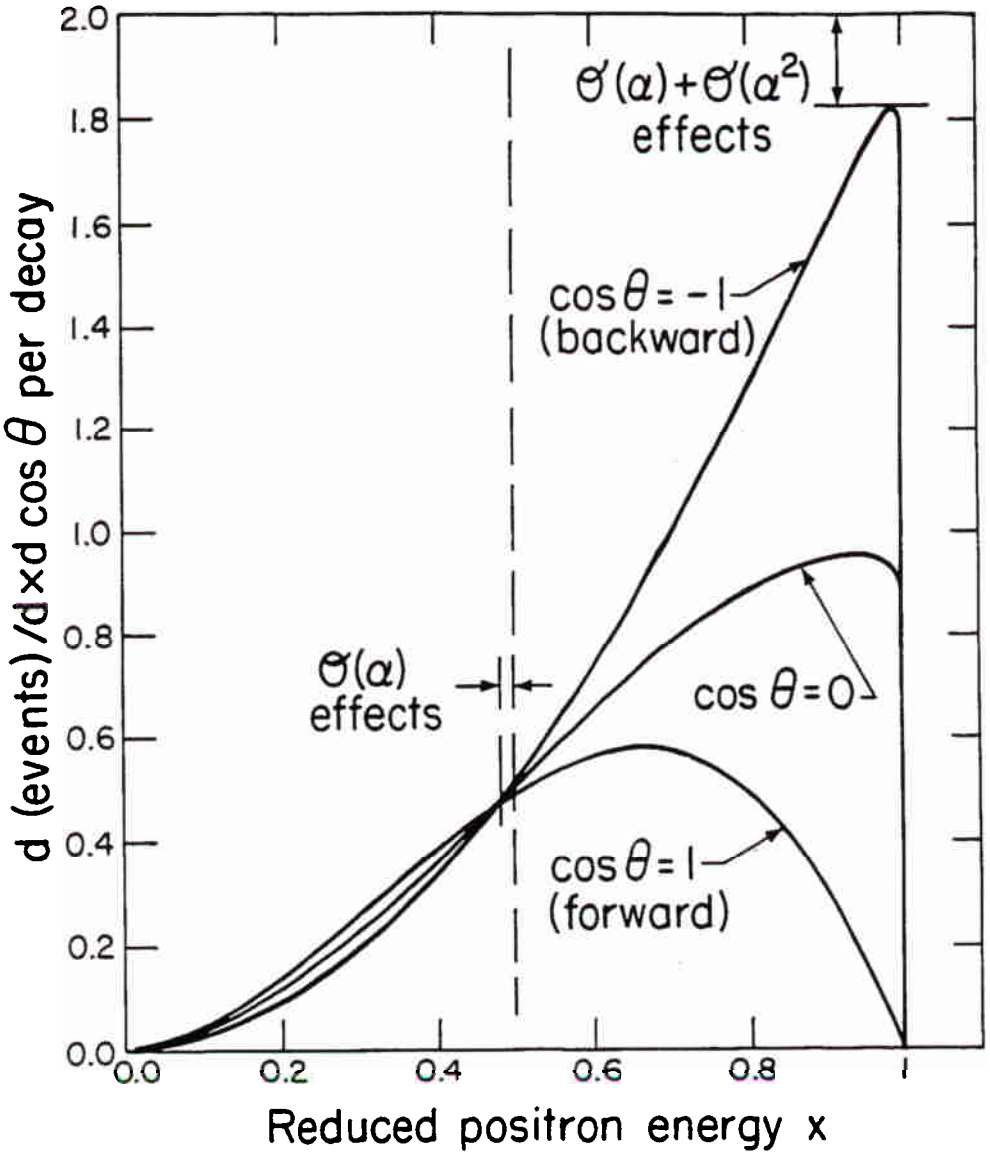

XBL 8512-11756

Fig. 2

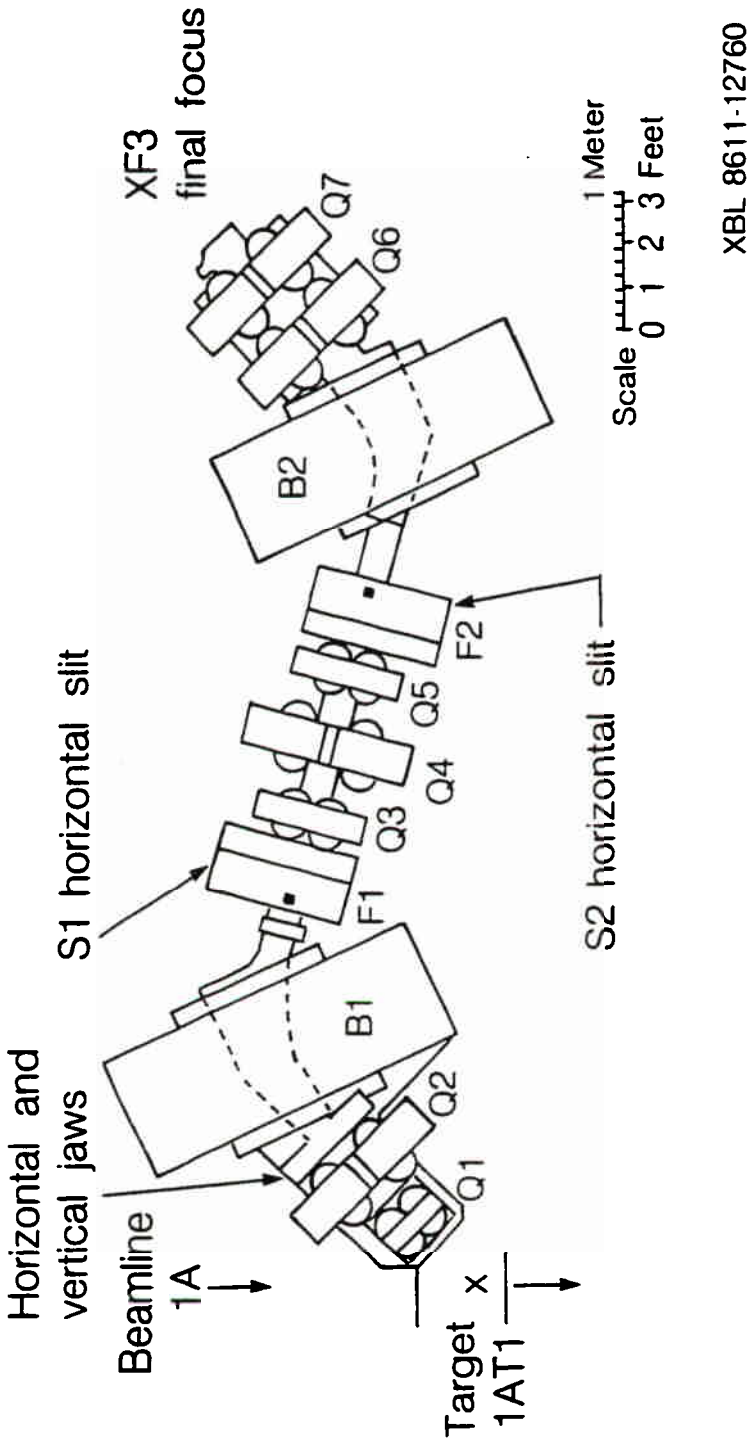
Horizontal and
vertical jaws
Beamline
1A
S1 horizontal slit
XF3
final focus
Q7
Q6
B2
B1
F1
Q3
Q4
Q5
F2
Q2
Q1
S2 horizontal slit
Target
1AT1
x
1 Meter
Scale
0 1 2 3 Feet
XBL 8611-12760

Fig. 3

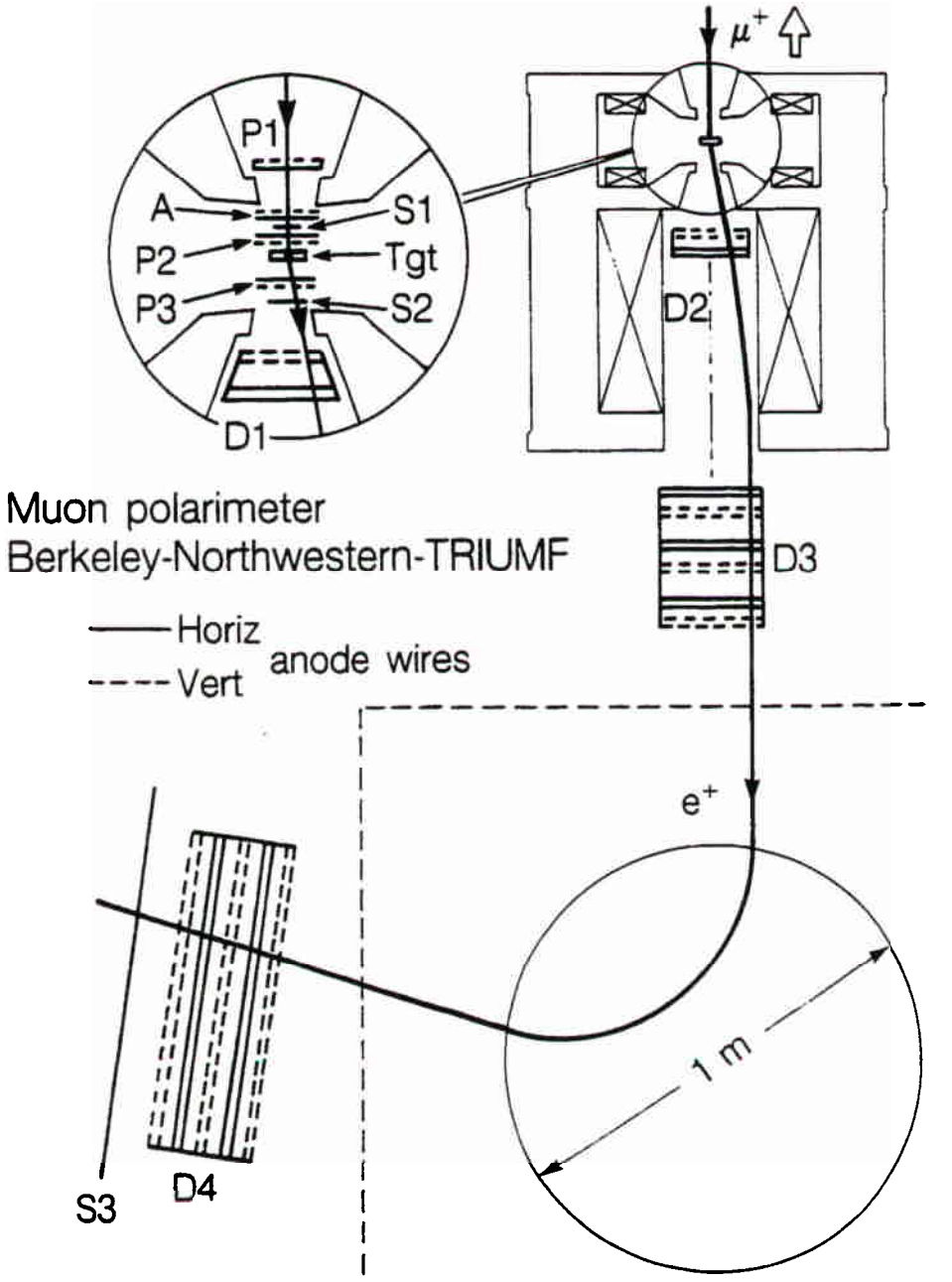

XBL 834-147A

Fig. 4

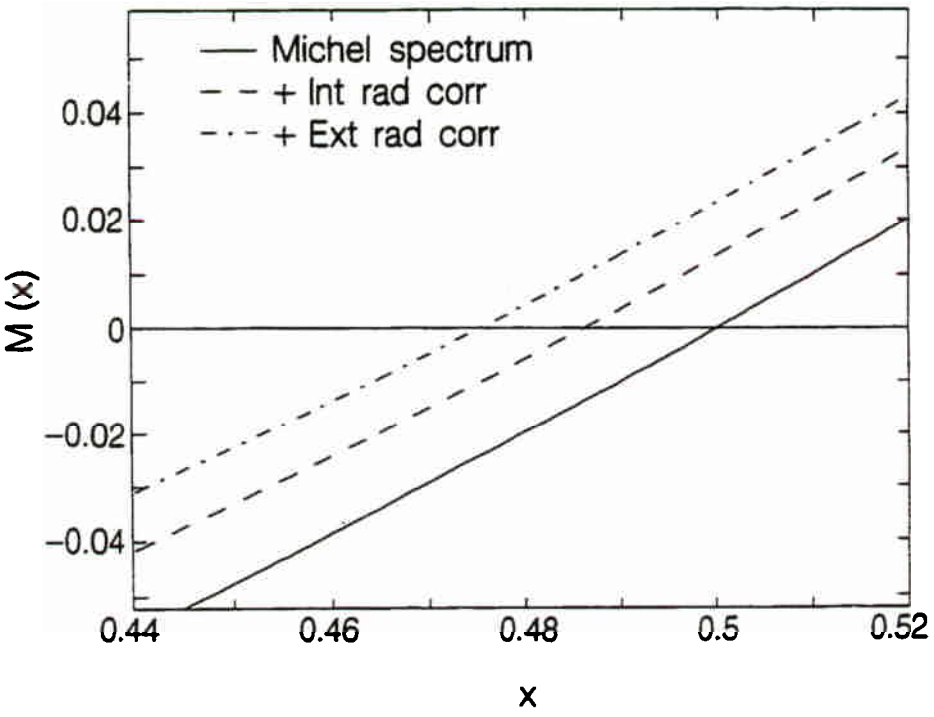

XBL 8611-11769

Fig. 5

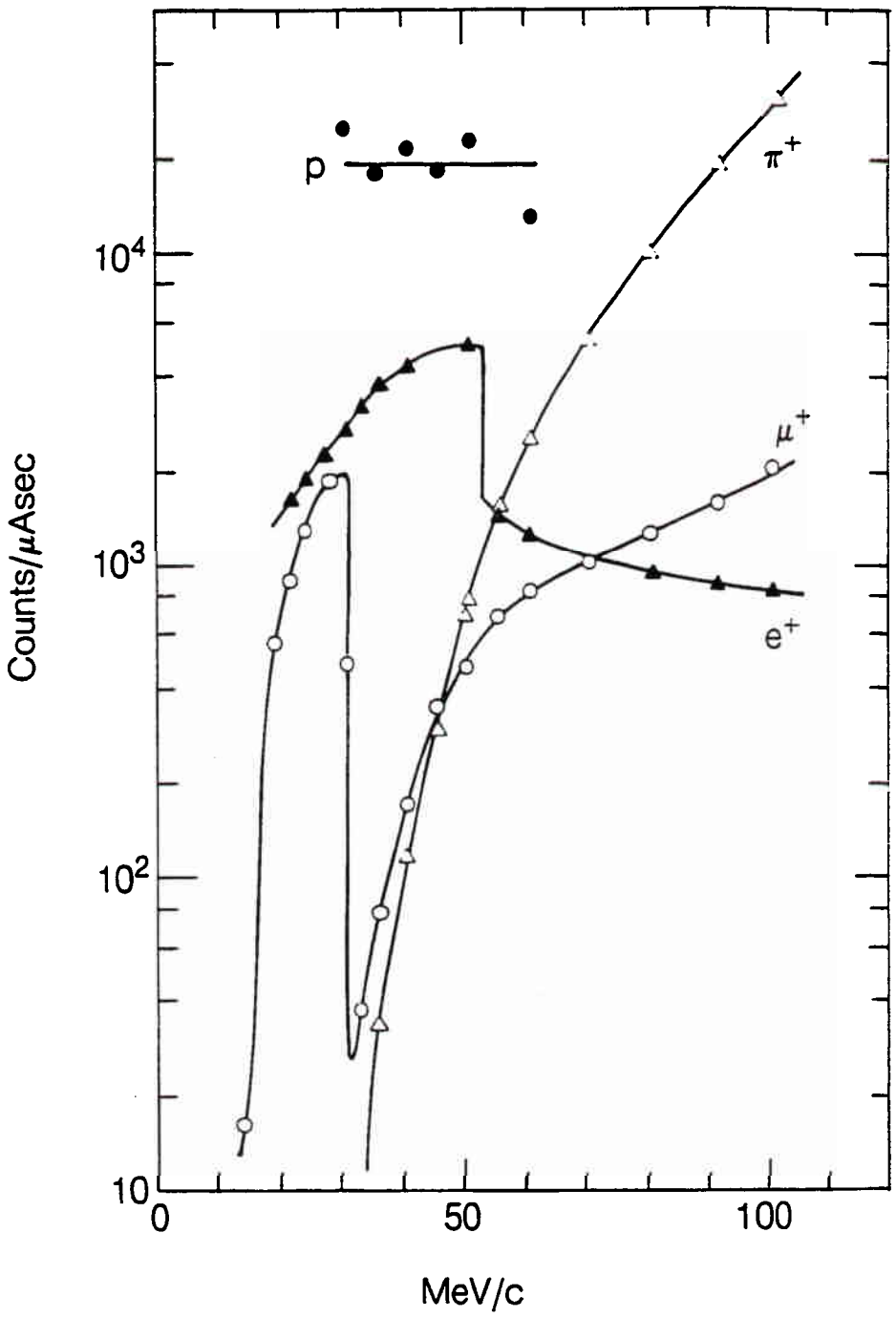

XBL 8611-12763

Fig. 6

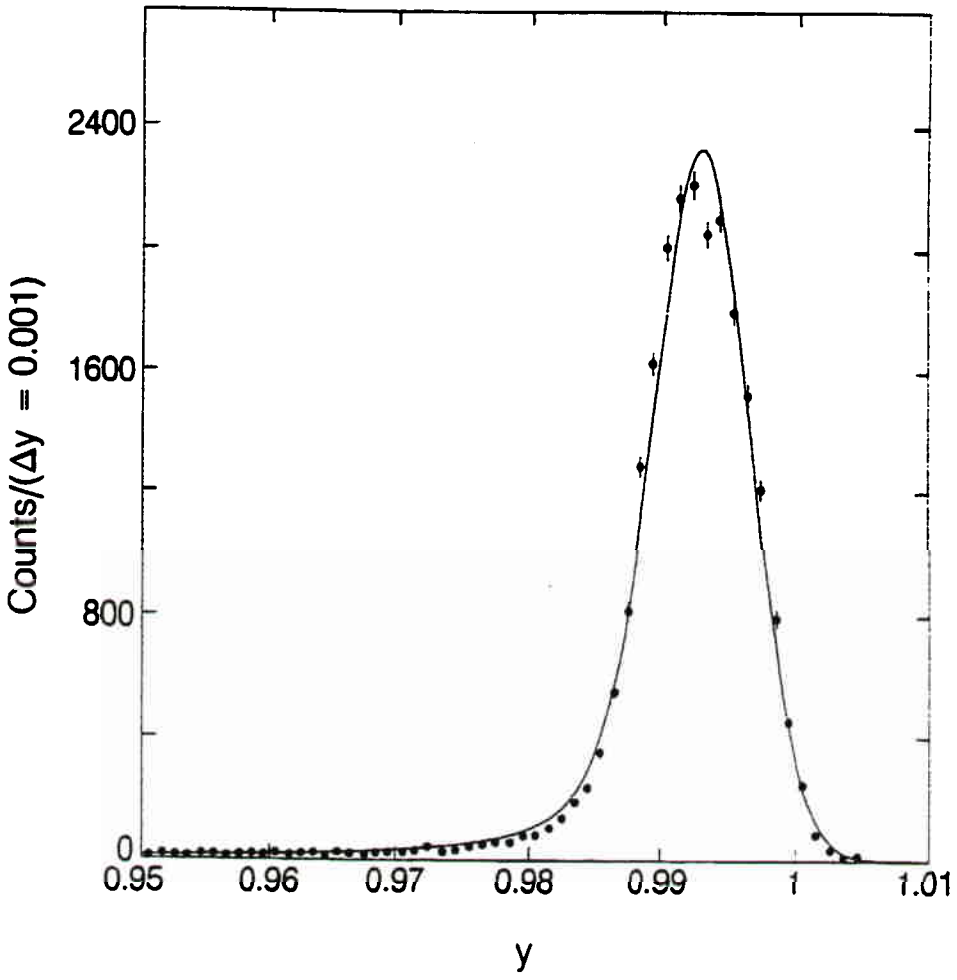

XBL 8611-12761

Fig. 7

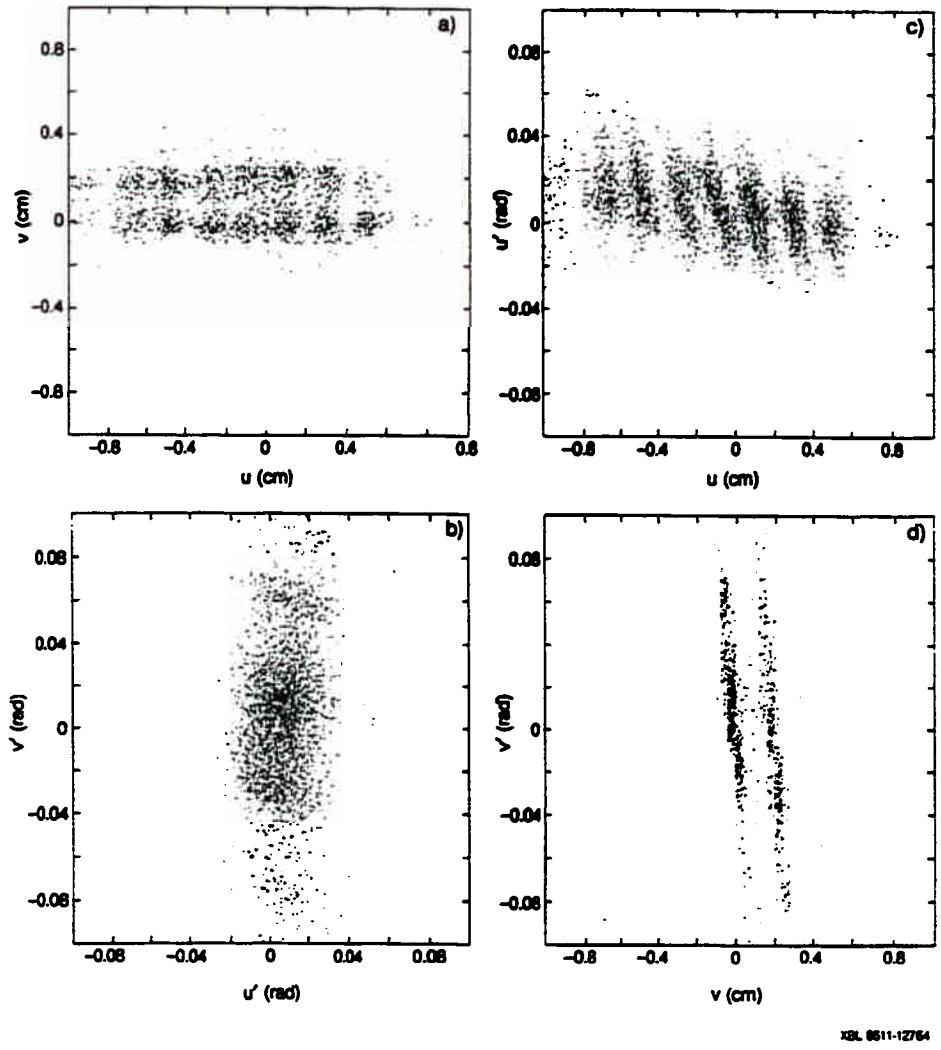
a)
c)
b)
d)
v (cm)
u (cm)
u' (rad)
v' (rad)
0.8
0.4
0
-0.4
-0.8
0.08
0.04
-0.04
-0.08
XBL 8511-12764

Fig. 8

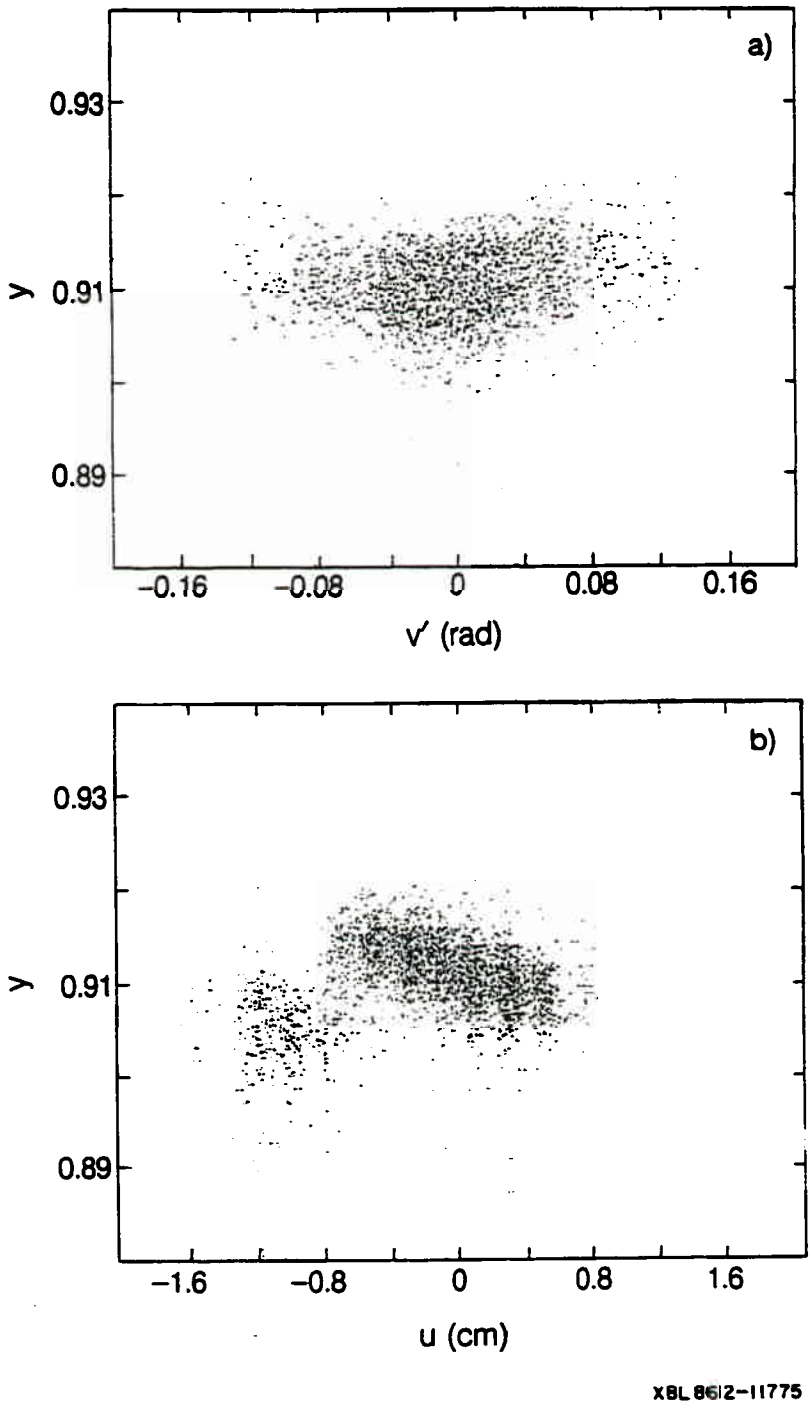
a)
0.93
0.91
0.89
y
-0.16
-0.08
0
0.08
0.16
v' (rad)
b)
0.93
0.91
0.89
y
-1.6
-0.8
0
0.8
1.6
u (cm)
XBL 8612-11775

Fig. 9

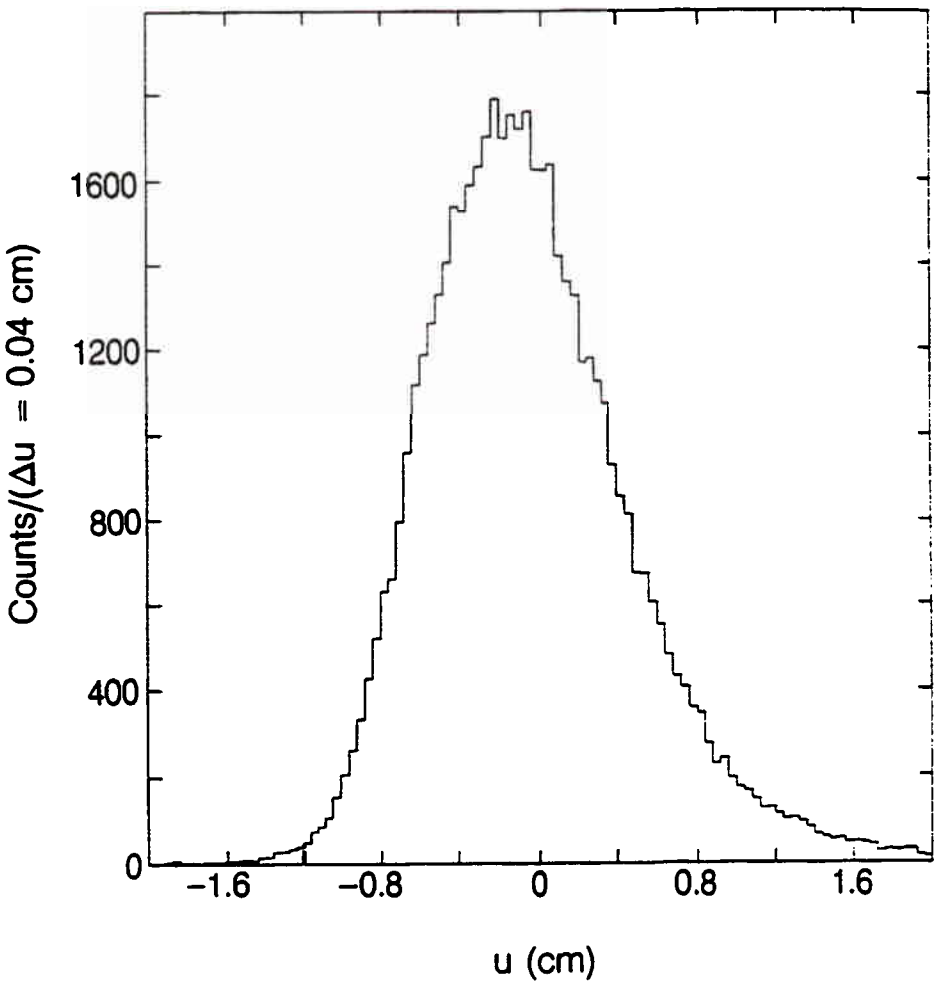

XBL 8611-12765

Fig. 10

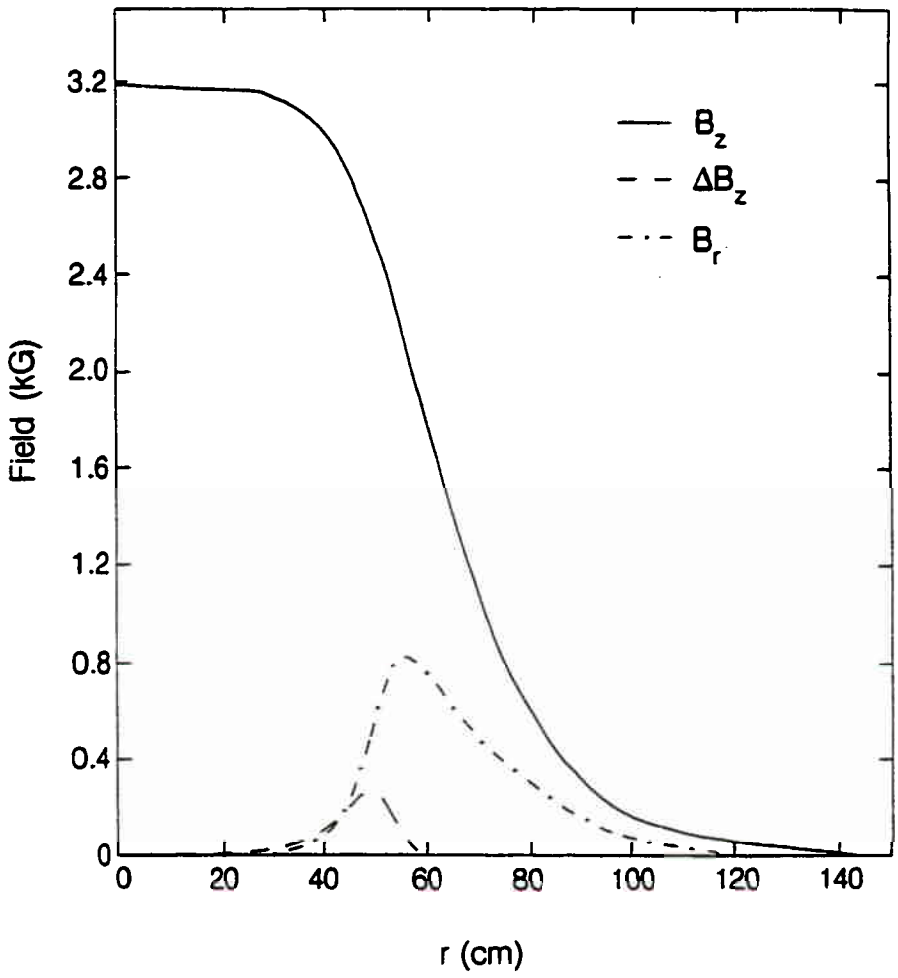

XBL 8611-11766

Fig. 11

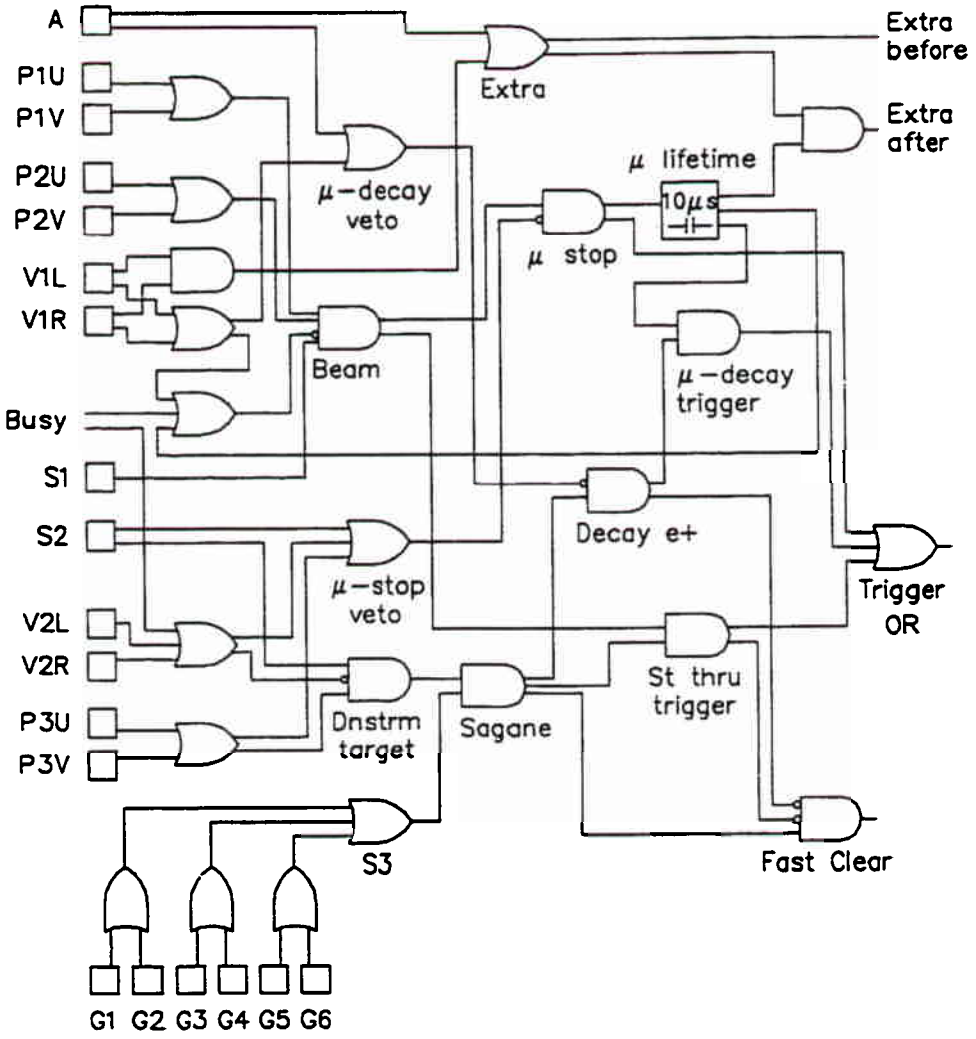

XBL 8611-12766

Fig. 12

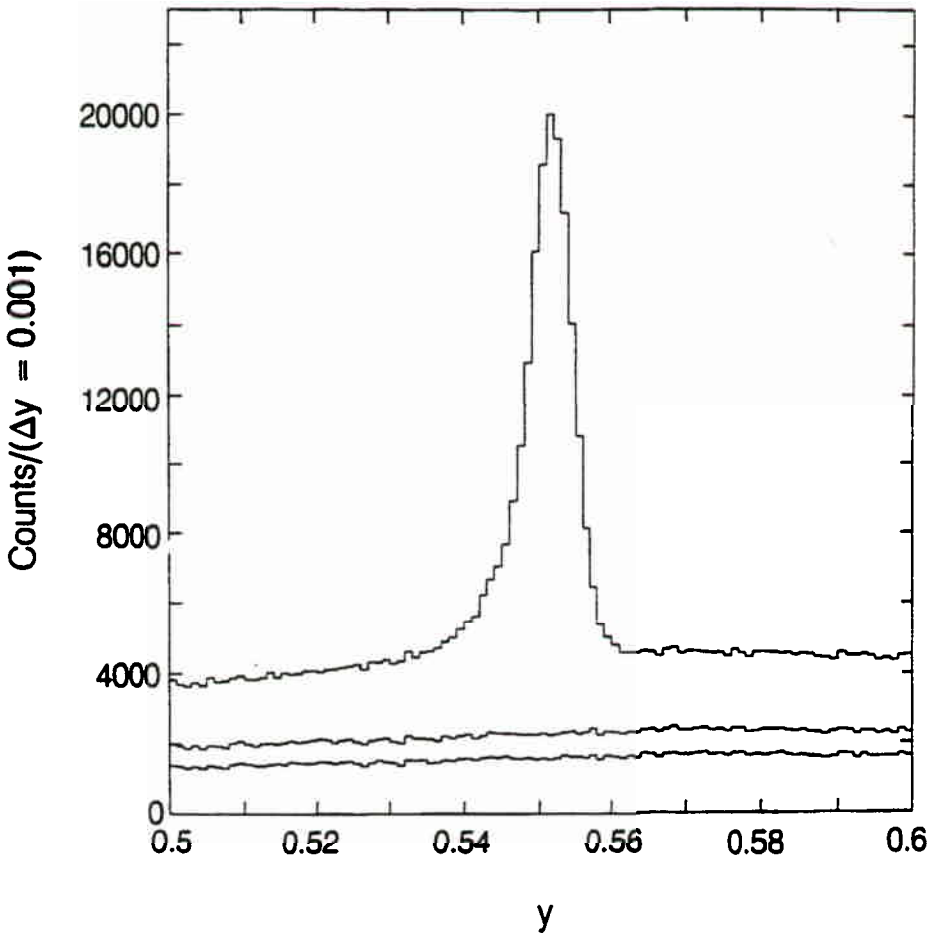

XBL 8611-11768

Fig. 13

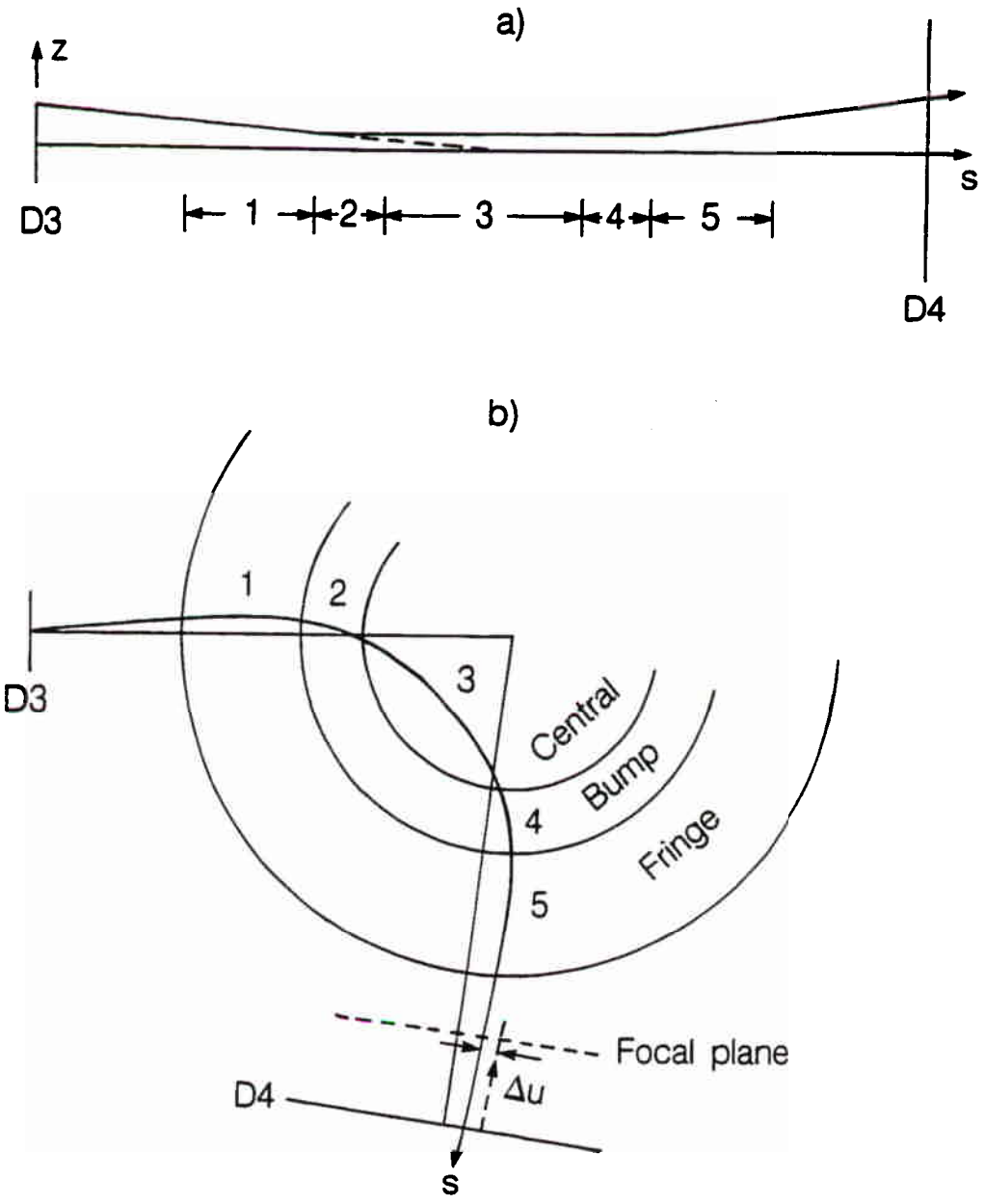

XBL 8612-11773

Fig. 14

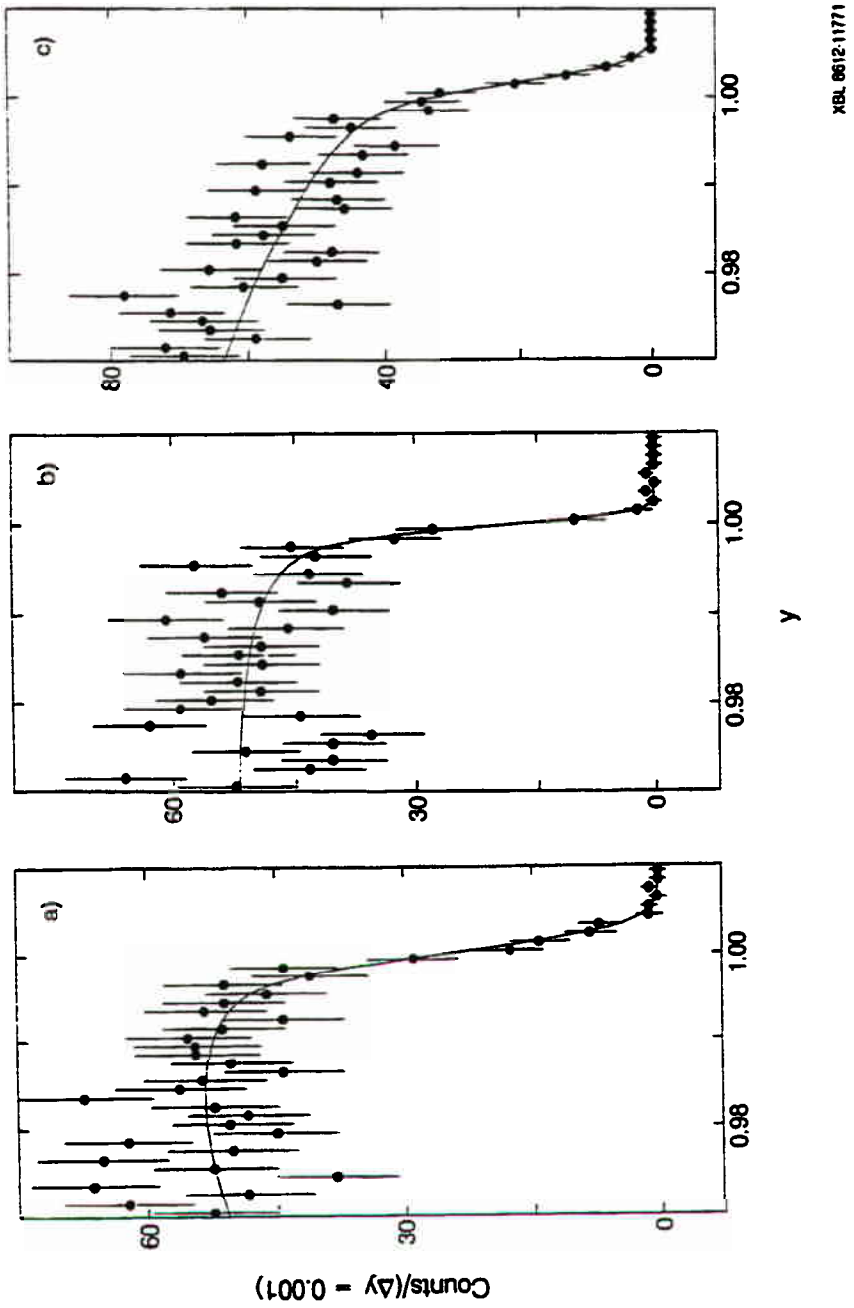

Fig. 15

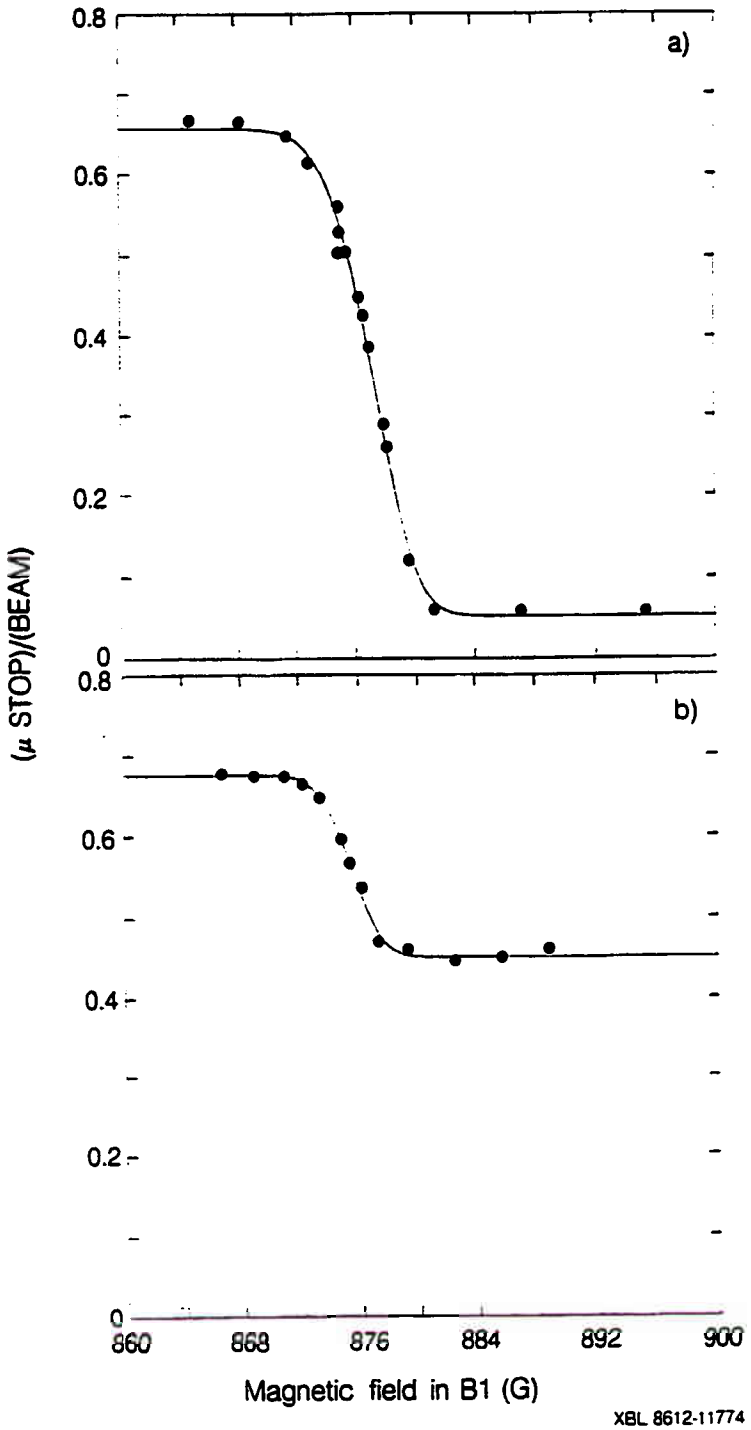
0.8
a)
0.6
0.4
0.2
0
0.8
b)
0.6
0.4
0.2
0
(μ STOP)/(BEAM)
860
868
876
884
892
900
Magnetic field in B1 (G)
XBL 8612-11774

Fig. 16

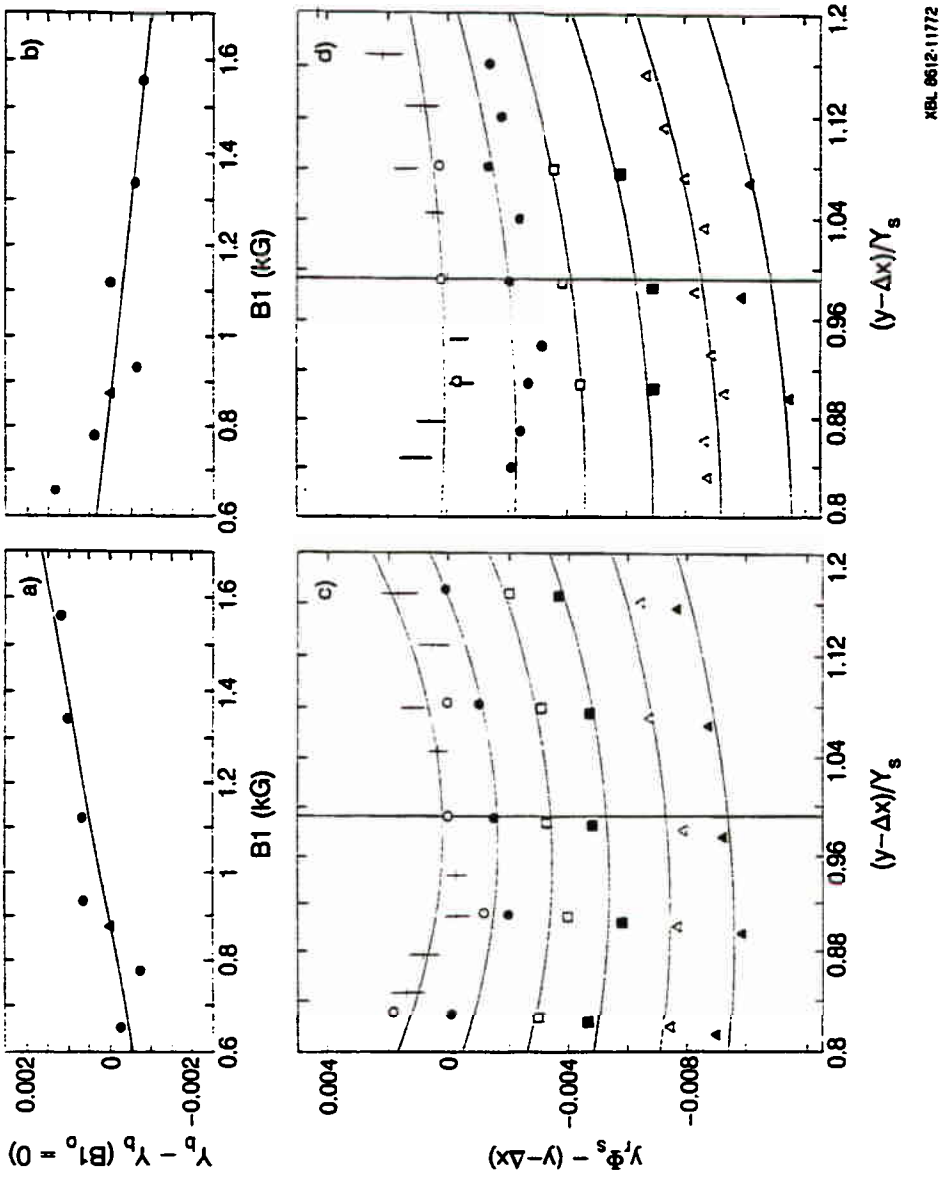
a)
b)
c)
d)
B1 (kG)
B1 (kG)
$(y-\Delta x)/Y_s$
$(y-\Delta x)/Y_s$
$Y_b - Y_b\ (B1_o = 0)$
$y'\Phi_s - (y-\Delta x)$
XBL 8612-11772

Fig. 17

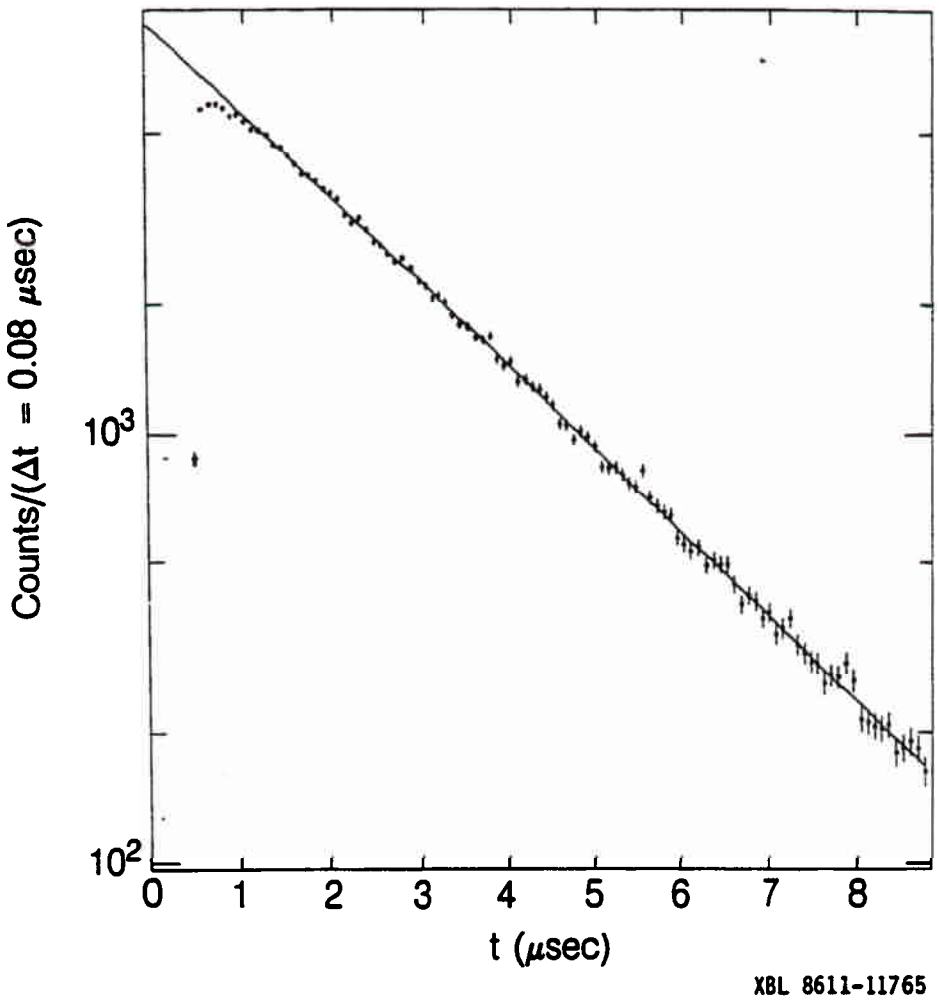

Fig. 18

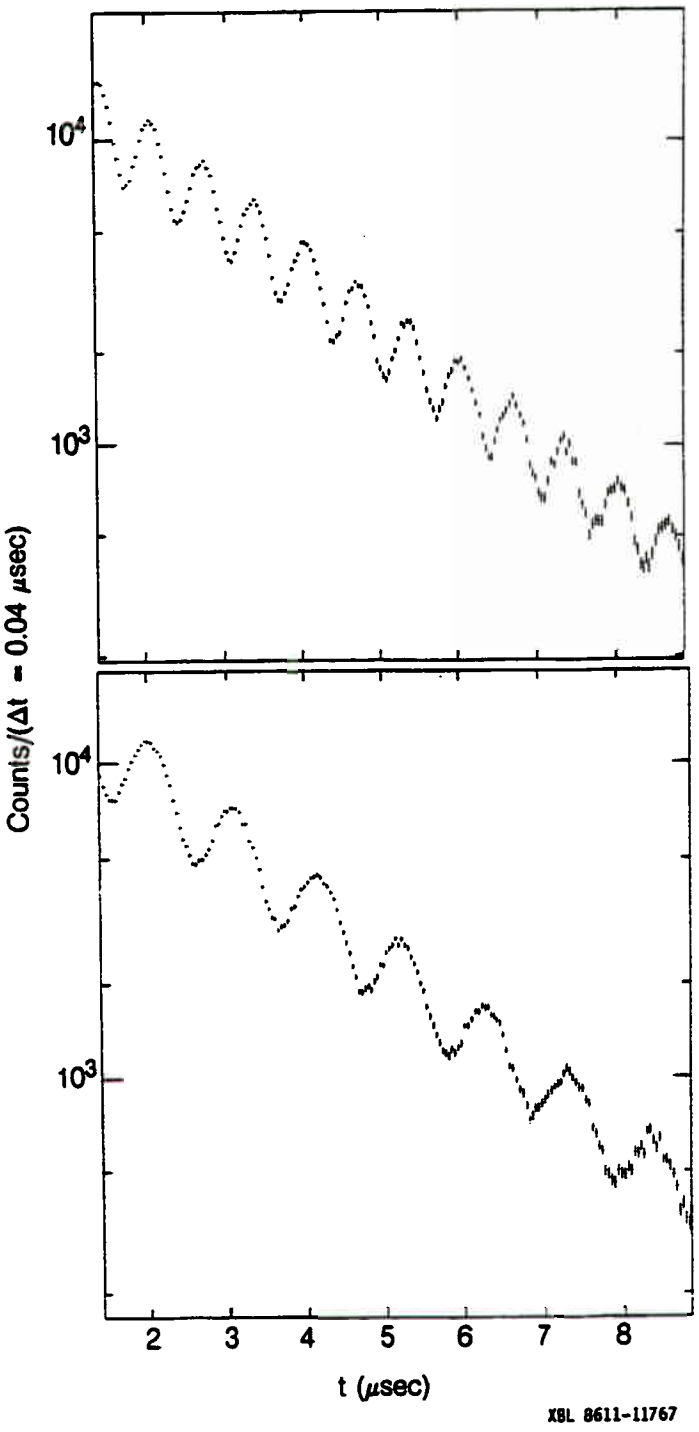
Counts/(Δt = 0.04 μsec)
10⁴
10³
10⁴
10³
2
3
4
5
6
7
8
t (μsec)
XBL 8611-11767

Fig. 19

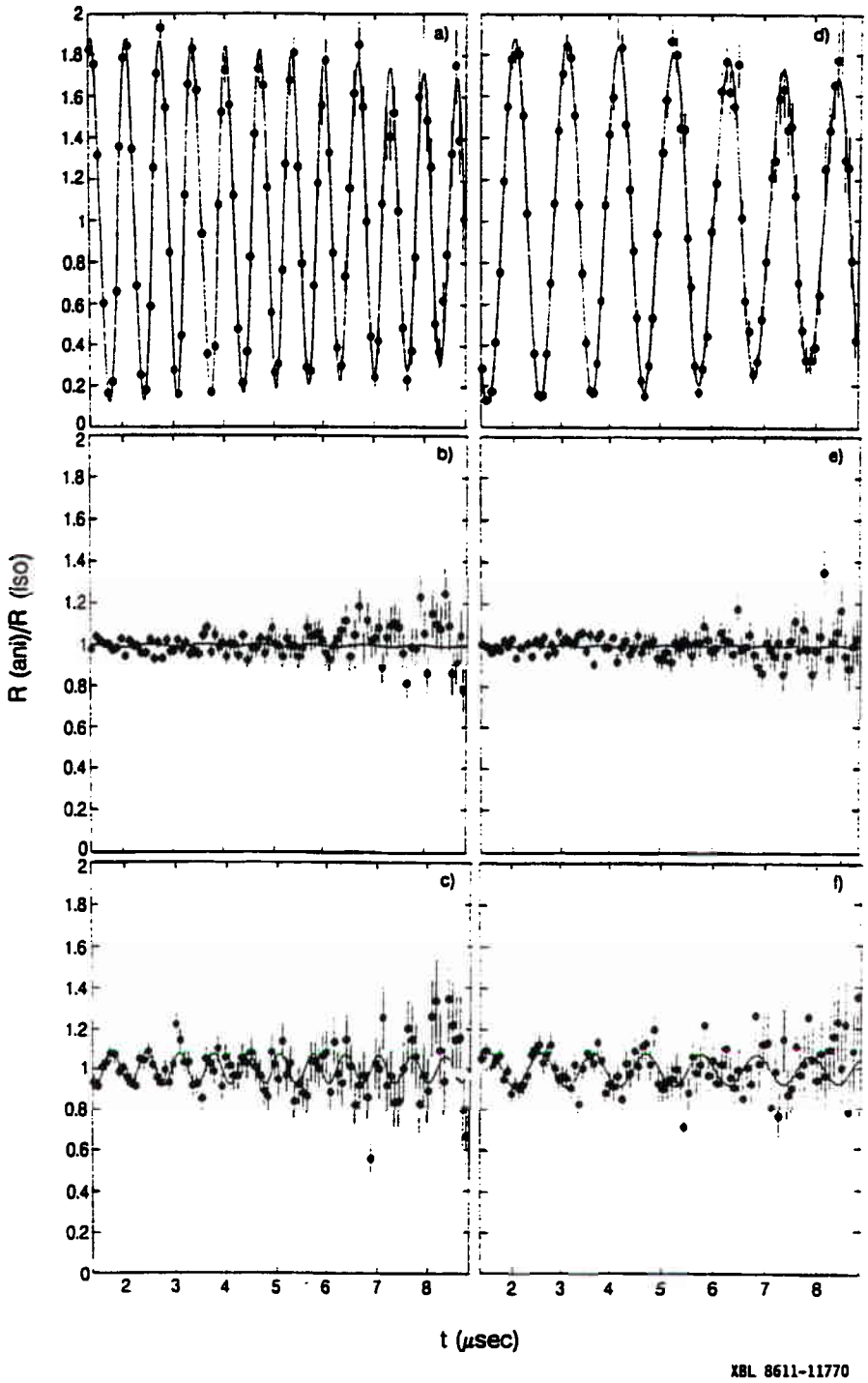

Fig. 20

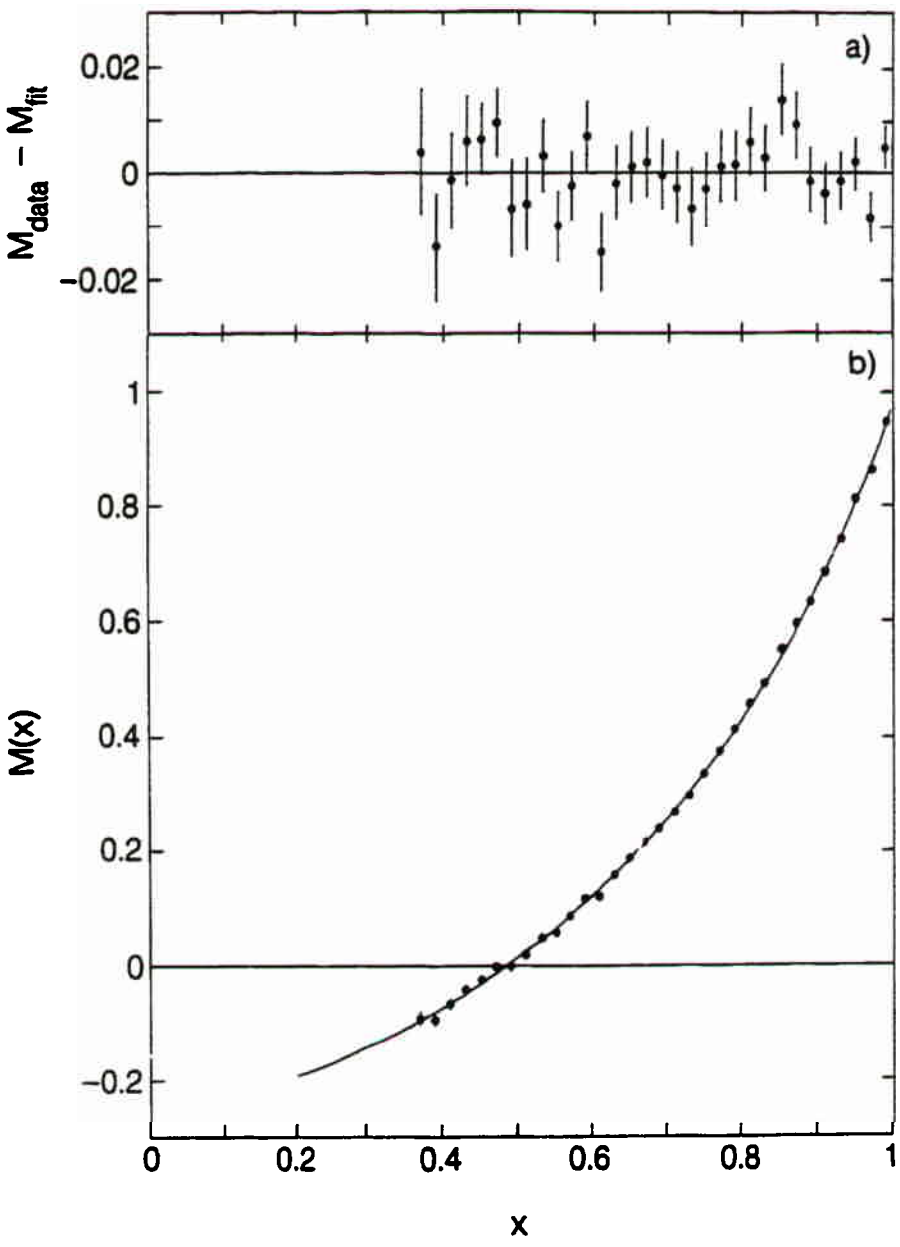

XBL 8611-12762

Fig. 21

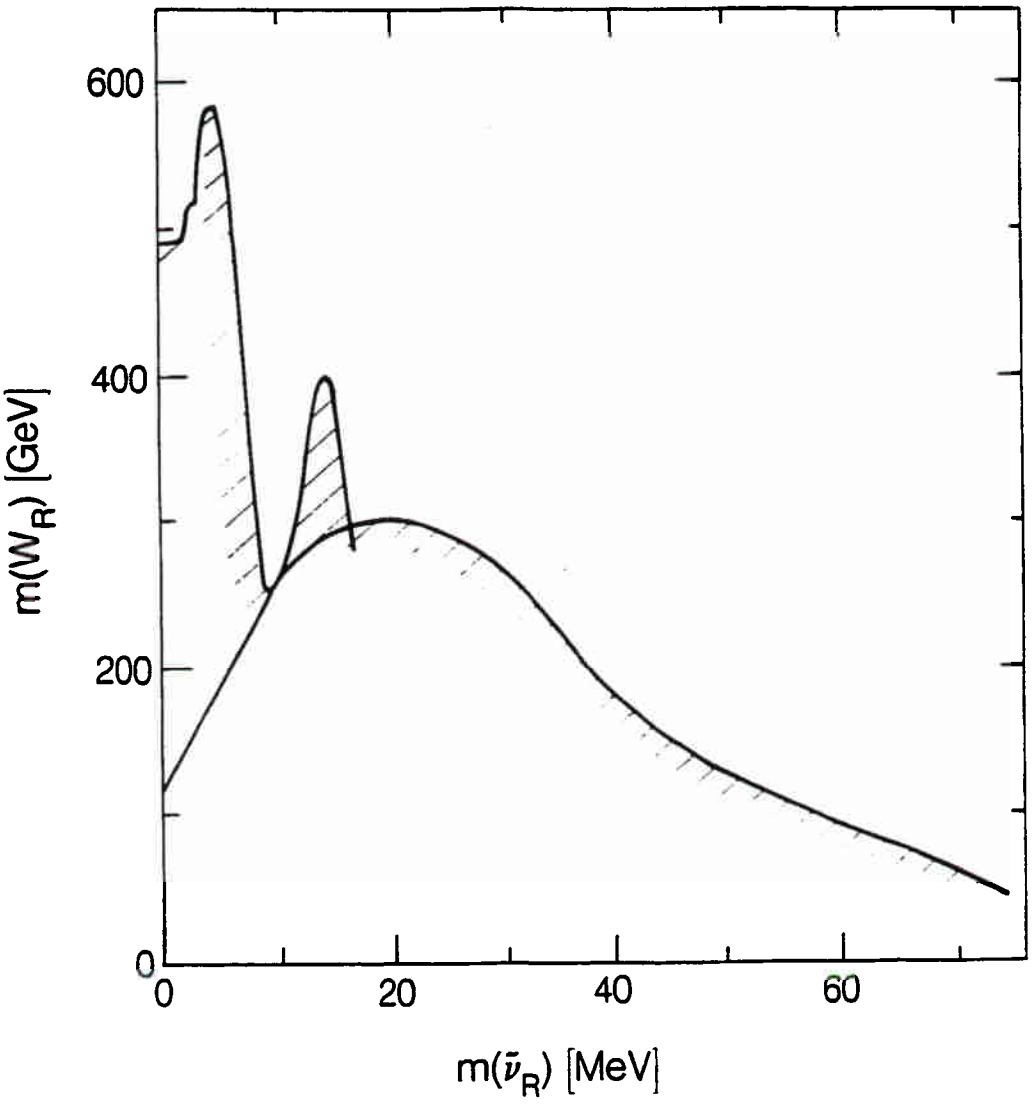

XBL 873-9615

Fig. 22

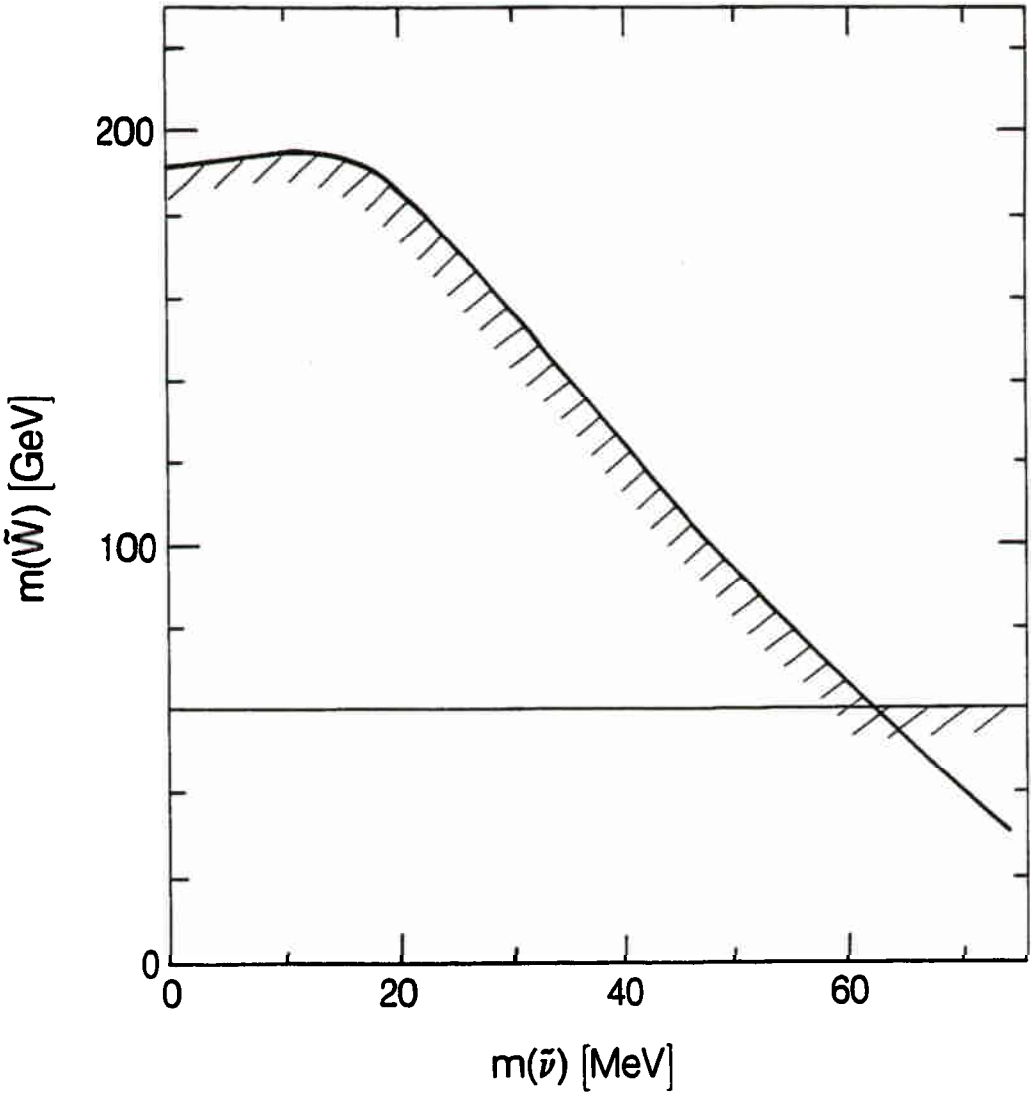

XBL 873-9617

Fig. 23

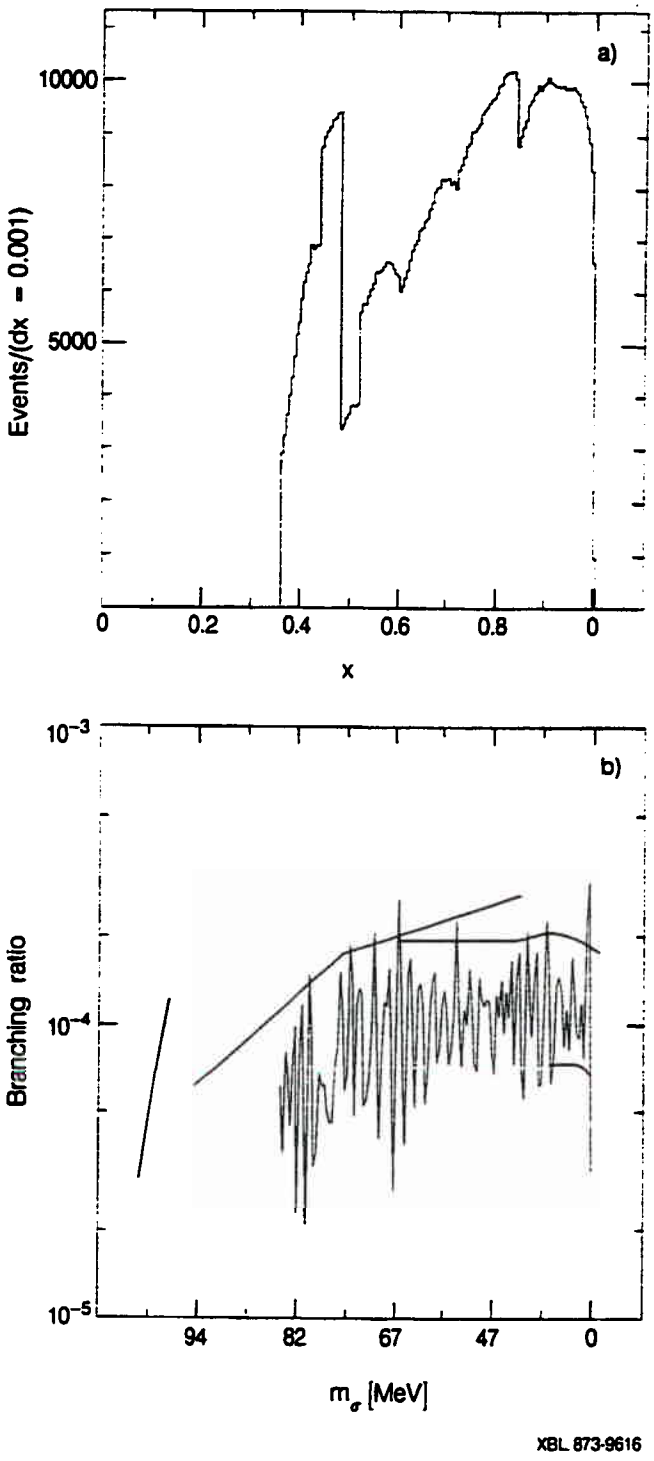
a)
10000
5000
Events/(dx = 0.001)
0
0.2
0.4
0.6
0.8
0
x
b)
10^{-3}
10^{-4}
10^{-5}
Branching ratio
94
82
67
47
0
m_σ [MeV]
XBL 873-9616

Fig. 24